Amyloids "at the border": deep mutagenesis and random sequence extension reveal an incomplete amyloid-forming motif in Bri2 that turns amyloidogenic upon C-terminal extension.

Mariano Martín[1] and Benedetta Bolognesi[1*]

[1]Institute for Bioengineering of Catalonia (IBEC), The Barcelona Institute of Science and Technology, Baldiri Reixac 10-12, 08028 Barcelona, Spain.

*Benedetta Bolognesi
Email: bbolognesi@ibecbarcelona.eu

Abstract

Stop-loss mutations cause over twenty different diseases. The effects of stop-loss mutations can have multiple consequences that are, however, hard to predict. Stop-loss in *ITM2B/BRI2* results in C-terminal extension of the encoded protein and, upon furin cleavage, in the production of two 34 amino acid long peptides, ADan and ABri, that accumulate as amyloids in the brains of patients affected by familial Danish and British Dementia. To systematically explore the consequences of Bri2 C-terminal extension, here, we measure amyloid formation for 676 ADan substitutions and identify the region that forms the putative amyloid core of ADan fibrils, located between positions 20 and 26, where stop-loss occurs. Moreover, we measure amyloid formation for ~18,000 random C-terminal extensions of Bri2 and find that ~32% of these sequences can nucleate amyloids. We find that the amino acid composition of these nucleating sequences varies with peptide length and that short extensions of 2 specific amino acids (Aliphatics, Aromatics and Cysteines) are sufficient to generate novel amyloid cores. Overall, our results show that the C-terminus of Bri2 contains an incomplete amyloid motif that can turn amyloidogenic upon extension. C-terminal extension with de novo formation of amyloid motifs may thus be a widespread pathogenic mechanism resulting from stop-loss, highlighting the importance of determining the impact of these mutations for other sequences across the genome.

Introduction

Frameshift mutations and stop-loss mutations make up ~0.2% of codon-changing mutations[1] and often result in mRNA degradation by the non-stop mediated-decay (NMD) machinery[2]. However, in the presence of an alternative in-frame stop codon within 50 nt from the original one, NMD is not triggered and aberrant proteins with an extended C-terminus can be expressed[1]. The C-terminal extension resulting from stop-loss can lead to both loss or gain of protein function[3–10]. with over 20 of these mutations proposed as causes of genetic disease[6].

The molecular mechanisms underlying pathogenicity of stop-loss mutations are diverse[3–10]. The extended protein products resulting from stop-loss can be depleted co- or post-translationally[3,4]. Stop-loss mutations in genes *PNPO, HSD3B2* and *SMAD4* for example produce a novel degron in the extended C-terminal and are targeted to the ubiquitin-proteasome system[5,6]. On the other hand, amorphous aggregates formed by C-terminal extensions of CEP97 are instead cleared by lysosomal degradation[3]. Other mechanisms of stop-loss pathogenicity include mislocalization, with C-terminal extensions causing the transcription factor MITF to mislocalize from the nucleus to the cytoplasm and rhodopsin to occupy different layers of the plasma membrane[7,8].

Finally, the physico-chemical properties encoded by extended sequences can occasionally lead to aggregation of the mutated protein into amyloid fibrils and thus cause or contribute to the pathogenicity induced by stop-loss mutations. Stop-loss mutations in *NEFH* and *REEP1* allow translation of 3' UTRs that contain amyloidogenic motifs, leading to protein aggregation and neurodegeneration in Charcott-Marie-Tooth disease and peripheral neuropathy, respectively[9,11]. *ITM2B*, also known as *BRI2*, is instead mutated in familial British (FBD)[10] and Danish Dementia (FDD)[12] and also encodes amyloids upon stop-loss. In the last three years, two additional stop-loss mutations in *ITM2B/BRI2* have been discovered, leading to Korean (FKD)[13] and Chinese Dementia (FCD)[14]. These examples suggest that cryptic amyloid formation could be a more general mechanism of pathogenicity induced by stop-loss and consequent C-terminal extension.

The C-terminus of the transmembrane protein encoded by *ITM2B/BRI2* is cleaved by furin, releasing the 23 amino acid long peptide known as Bri2 (Fig. 1a). Upon stop-loss mutations, furin cleavage produces aberrant 34 amino acid long peptides with distinct amino acid sequences in different types of dementia (Fig. 1b). In FBD, stop-loss results from a single nucleotide variant (SNV), c.799T>A, and produces a peptide known as ABri[10]. FCD and FKD mutations (c.800G>C and c.800G>T, respectively) generate peptides that differ from ABri only in one amino acid at position 24 of the extended peptide (Fig. 1b)[13,14]. In FDD, a 10 nt duplication (c.795-796insTTTAATTTGT) that causes frameshifting and stop loss, leads to an aberrant peptide known as ADan, whose last 12 residues are entirely distinct from ABri (Fig. 1b)[12]. Thus, multiple C-terminal extensions of Bri2 peptide can lead to amyloid formation in the context of autosomal dementia, suggesting that the Bri2 sequence holds an amyloid potential which can be unlocked by specific peptide extensions.

Here, we employ deep mutational scanning (DMS) to scan the impact of all ADan mutations on amyloid nucleation so to identify the putative amyloid core formed by this peptide. To then explore how likely C-terminal extension in *ITM2B/BRI2* is to generate amyloid cores we use random

sequence extension (RSE) and systematically measure the consequences of ~18,000 random C-terminal extensions of Bri2. Our massive dataset reveals that a large fraction (~32%) of these extended peptides nucleate amyloids. Among the strongest nucleators we find C-terminal extensions of just two amino acids. We further find that the novel amyloids display specific amino acid enrichments that depend on sequence length.

Altogether, our results suggest that the C-terminus of Bri2 contains an incomplete amyloid motif that can turn amyloidogenic upon extension. They also demonstrate that massively parallel quantitative assays, such as the one presented here, provide a robust strategy to map amyloid formation from novel areas of the sequence space and that they can generate valuable insights into the general consequences of C-terminal extension arising from mutations, drug-induced readthrough or aberrant 3' UTR translation.

Results

Quantifying amyloid nucleation of Bri2 extensions

To measure the ability of Bri2 extensions to nucleate amyloid aggregates we employed a cell-based selection assay where sequences are fused to the nucleation domain of the yeast prion Sup35 (SupN) and amyloid nucleation of the fused peptides seeds the aggregation of endogenous Sup35 (Supp. Fig. 1a)[15]. This process is required for yeast growth in selective conditions and we previously showed that growth rates in this assay correlate with rates of amyloid nucleation in a test tube[16].

Cells expressing Bri2 do not grow in these conditions, revealing that the unextended peptide does not nucleate amyloid aggregation (Fig. 1c). In sharp contrast, the expression of ADan leads to 25.14 ± 3.41% of the cells growing in selection media over non-selective conditions, a 2-fold increase compared to the growth rate induced in the same conditions by the amyloid-beta peptide (Aβ42), the peptide that forms amyloids in Alzheimer's disease and is mutated in familial forms of the disease[16] (Fig. 1c, Supp. Fig. 1b). Cells expressing ABri fusions show very limited growth in the assay (0.0065 ± 0.0039%) with no significant difference compared to expression of the reporter without any fusion (SupN) (Fig. 1c, Supp. Fig. 1b). Growth assays of cells expressing Bri2, ABri or ADan fusions in non-selective conditions revealed that their growth rates were not confounded by differential toxicity (Supp. Fig. 1c).

Quantifying the effect of ADan substitutions and truncations on amyloid nucleation at scale

To further investigate the sequence-nucleation landscape of the ADan peptide we designed and synthesized a library containing all ADan single amino acid substitutions and truncations (n=680), and expressed it fused to SupN in yeast cells that went under selection as above (Supp. Fig. 1a). We quantified growth rates and therefore amyloid nucleation for each variant in the library by deep sequencing before and after selection (Fig. 1d)[16]. Growth rates, henceforth "nucleation scores",

from this high throughput assay were reproducible between replicates (Fig. 1e, Supp. Fig. 1d) and correlate well with the effects of variants quantified individually (Pearson Correlation, R = 0.94, p-value: 5.3e-3; Fig. 1f). Altogether, we measured amyloid nucleation for 642 single amino acid substitutions (99% of possible amino acid substitutions) and all 34 truncations. In this dataset, synonymous mutations have a nucleation score close to 0, i.e similar to WT ADan, nonsense variants (truncations) have a unimodal distribution with a peak at a nucleation score of ~-4 and the distribution of missense variants (amino acid substitutions) has a strong bias towards reduced amyloid nucleation (Fig. 1g).

A four amino acid extension of Bri2 has the same propensity to nucleate amyloids than the full length ADan peptide

Pathogenic Bri2 extensions share the first 22 residues and differ only in the last 12 amino acids (Fig. 1b), suggesting it is the specific extension of ADan that encodes amyloid potential. Measuring the nucleation score of all possible ADan C-terminal truncations in our library, we find that a truncated version of ADan ending at position 25 (equivalent to an extension of Bri2 by F23, N24 and L25) nucleates amyloids significantly faster than Bri2 (Fig. 1h; Z-test, false discovery rate [FDR] = 0.01, p-adjusted: 1.038e-297, Benjamini & Hochberg correction). This effect becomes stronger with a peptide of 26 amino acids (Bri2 extension by F23, N24, L25 and F26), leading to a similar nucleation score as that of the full-length ADan peptide (Z-test, false discovery rate [FDR] = 0.01, p-adjusted: 1.544e-02, Benjamini & Hochberg correction). Together with the previous observation that a 28 residue long ADan truncation forms beta-sheet rich aggregates *in vitro*[17], these findings suggest that the amyloid potential of ADan is encoded by the first residues that get translated upon stop-loss.

Deep mutagenesis of ADan uncovers its amyloid core and residues that act as gatekeepers of amyloid nucleation

The distribution of mutational effects for ADan nucleation reveals that 44% of single amino acids substitutions reduce nucleation and only 25% increase it (Z-test, false discovery rate [FDR] = 0.1, Fig. 2a) while 30% of these variants have a nucleation score similar to WT ADan.

Inspecting the heatmap of mutational effects for amino acid changes at all positions in ADan reveals that 26% of the mutations that decrease amyloid nucleation are localized in a short region of 7 amino acids between residues L20-F26 (Fig. 2b, Supp. Fig. 3a). In this continuous stretch of residues most mutations decrease amyloid nucleation (an average of 55% of mutations per position decrease nucleation) and all substitutions to prolines disrupt it (except for L20P that increase nucleation and N24P that is WT-like), suggesting tight structural constraints (Fig. 2b, Supp. Fig. 3a). Thus, we propose that this region forms the inner core of the nucleating ADan fibrils and assign a key role in this process to N24 as all mutations (except N24P) at this position lead to a decrease in nucleation. Charges in this stretch are not tolerated, except at position 23 and change F26E. Outside of this region, at positions E18, T19, N4 and E31, mutations to hydrophobic amino acids decrease nucleation, suggesting longer distance interactions with residues of the amyloid core or a role in modulating the conformations of the monomeric ADan ensemble. Overall, asparagines and glutamic acids are key in ADan nucleation as most

144 substitutions of these amino acids decrease nucleation (75% and 71% of substitutions decrease
145 nucleation, respectively; Fig. 2c).

146 We identify five gatekeepers, positions where mutations are more likely to increase nucleation
147 than decrease it[18–20]: F6 (12 mutations increasing nucleation and 2 decreasing), I8 (15
148 increasing), K14 (11 increasing and 2 decreasing), A16 (12 increasing and 5 decreasing) and L27
149 (11 increasing and 3 decreasing) (Fig.2e). Surprisingly, and in contrast to what was previously
150 found for other amyloids[18–20], including Aβ42[16,21], 4 out of 5 gatekeepers are aliphatic residues
151 except for K14.

152 We also find that 7 of the reported SNPs in *ITM2B/BRI2* (GnomAD database[22]) decrease
153 nucleation, 10 do not affect nucleation and only 1 of them (rs1272422512), which results in
154 mutation R9Q, increases the nucleation of the ADan peptide (Fig. 2b, Supp. Table 1). However,
155 we identify another 53 SNVs that significantly increase nucleation in ADan (Fig. 2b, Supp. Fig.
156 3a).

157 **Multiple *ITM2B/BRI2* stop-loss mutations increase nucleation**

158 We then employed the same strategy to test whether specific genetic variants in ABri can boost
159 its weak amyloid nucleation propensity. After data processing and filtering (see methods and
160 Supp. Fig. 2a), we found 121 variants that were able to increase nucleation (Supp. Fig. 2 and
161 Supp. Fig. 3b). The heatmap of mutational effects for amino acid changes at all positions in ABri
162 reveals that substitutions R24L and R24S increase nucleation (Supp. Fig. 2d and Supp. Fig. 3b),
163 meaning that the peptides that are a product of FCD and FKD mutations are more prone to
164 aggregate than both Bri2 and ABri. Moreover, the R24C mutation, equivalent to a single stop-loss
165 mutation leading to a Cys codon (c.801A>C: TGA>TGC or c.801A>T: TGA>TGT), significantly
166 increases nucleation (Supp. Fig. 2b,d and Supp. Fig. 3b). Also, substitution by Cys at position 20
167 (L20C) significantly increases nucleation, inducing a relative growth in selection media over non-
168 selective conditions of 63.1 ± 7.1%, that is 2.7 times more than ADan peptide nucleation (23.1 ±
169 3.6%).

170 **Different types of mutations increase the nucleation of ADan, ABri and Aβ42 amyloids**

171 As Alzheimer's disease and *ITM2B/BRI2*-related familial dementias share common clinical and
172 neuropathological features, including amyloid depositions[12,23–25], we evaluated if the impact of
173 mutations on amyloid nucleation of ADan depends on similar properties as those driving Aβ42
174 nucleation. There is no significant correlation between the nucleation scores of variants in these
175 peptides when comparing mutations of the same amino acids (Fig. 3a) or mutations to the same
176 amino acid (Fig. 3b). In addition, to compare mutational effects by position, we aligned ADan and
177 Aβ42 peptides in three different ways, at the N-terminal, C-terminal and with ClustalO[26].
178 Regardless of the strategy, no significant correlation at the aligned positions was detected (Supp.
179 Fig. 4a,b,c).

180 Similarly, we compared ADan and ABri nucleation scores. None of the comparisons between
181 ADan and ABri revealed significant correlations between the nucleation scores of these peptides

182 (Fig. 3c,d; Supp. Fig. 4d). We also tested the correlation in those positions with at least 5 confident
183 measurements in the ABri library, uncovering significant positive correlations only for positions 13
184 (N), 26 (F and V) and 32 (K and E, ADan and ABri respectively; Fig. 3E).

185 Surprisingly, changes in hydrophobicity can explain very little of the variance in the ADan dataset
186 (Supp. Fig. 5a). Moreover, state-of-the-art amyloid predictors scores poorly correlate with ADan
187 nucleation scores (Supp. Fig. 5a) and analysis of the net and total charge of ADan variants gives
188 little insight in the process of ADan amyloid nucleation (Supp. Fig. 5b).

189 **Bri2 random extensions reveal the properties of de novo amyloid nucleating peptides**

190 To better understand the sequence determinants of amyloid core generation upon Bri2 C-terminal
191 extension, we generated three libraries where the Bri2 peptide (22 amino acids) is extended by
192 12 random degenerate (NNK, where N = A/C/G/T and K = G/T) codons, in a way that is similar to
193 what happens in ADan biogenesis (ADan-like extensions, Fig. 4A). Each library was selected
194 independently, and sequencing was used to quantify the relative amyloid nucleation scores for a
195 total of 17,952 unique amino acid sequences corresponding to 4.68e-18 of the possible sequence
196 space (20^{12}) (Fig. 4b and Supp. Fig. 6a). The β-sheet propensity and hydrophobicity, relevant
197 features in amyloid nucleation, of this experimental sequence space overlap with those of the
198 human proteome (Fig. 4d). After data processing and quality control, the vast majority of
199 sequences had a nucleation score of 0. Consequently, we classified sequences with a nucleation
200 score significantly greater than 0 as nucleators (n=5,678; 31.6% of the sequences; Z-test, false
201 discovery rate [FDR] = 0.05), and all other sequences as non-nucleators (n=12,274; 68.4%; Fig.
202 4b). The resulting nucleation scores correlate well with the effect of sequences quantified
203 individually (Fig. 4c).

204 We examined the differences in amino acid frequency between nucleating and non-nucleating
205 sequences with an extension of 12 amino acids (Fig. 4e). Although the differences were modest,
206 several of these were statistically significant (t-test), owing to the large sample size of our data.
207 The most relevant differences are in Asn (p-value=4.28e-56, Cohen's d effect size=0.30,
208 difference in frequency=1.50), Cys (p-value=6.69e-110, effect size=0.43, difference=2.71) and
209 Arg (p-value=5.23e-30, effect size=0.22, difference=-1.87; Fig. 4e; Supp. Fig. 6c; Supp. Table 2).
210 We also analyzed the amino-acid composition position-wise, finding that towards the N-terminus
211 of the extension (close to the end of the Bri2 sequence) nucleators are significantly enriched (chi-
212 squared test) in polar residues (Fig. 4f,g; min. p-value position 24=3.53e-11, Cohen's d effect
213 size=0.25, difference in frequency=0.056), Cys, Phe and/or Val (Fig. 4f, Supp. Fig. 6c; Supp.
214 Table 3). They are instead depleted in charged residues and aliphatics (Fig. 4f,g; Supp. Table 4).
215 The enrichment in polars and Cys is maintained all along the whole extension while the depletion
216 in aliphatics becomes even stronger towards the C-terminus (Fig. 4f,g; Supp. Table 4). In addition,
217 at the C-terminus, nucleators are enriched in Gly (Fig. 4f,g; min. p-value position 33=1.54e-5,
218 effect size=0), aromatics as well as positive and negative charges (Fig. 4f,g; Supp. Table 4).

219 Among the random C-terminal extensions, 1,824 sequences (~10% of the total) have a Ser
220 residue at position 23, mimicking the effect of stop-loss mutations that lead to production of ABri
221 and effectively generating a subset of ABri-like extensions. We performed the same amino acid

enrichment analysis on this subset of extensions, finding similar results as the ones found for all the other random extensions (Supp. Fig. 7).

We next evaluated if common amyloid aggregation predictors are able to predict the nucleation of these sequences and if they can discriminate between non-nucleatores and nucleators (Supp. Fig. 8a), or between non-nucleators and the 10% strongest nucleators in each random library (Supp. Fig. 8b). All of the predictors show a poor or limited performance on the prediction task (Supp. Fig. 8). In both cases CamSol outperforms the rest of the predictors with an AUC of 0.5660±0.0086 for discriminating non-nucleators versus nucleators and an AUC of 0.6482±0.0154 for non-nucleators versus the 10% strongest nucleators.

Bri2 extensions of two specific amino acids are sufficient to nucleate amyloids

Our random libraries also included shorter C-terminal extensions due to premature stop codons in the 12 degenerate-codon sequence (Fig. 5a; number of sequences with an extension < 12 amino acids: 5,110). We analyzed these sequences and found that the resulting peptide length is not correlated with the strength of amyloid nucleation (Fig. 5b). Moreover, we found that extending Bri2 by only two specific amino acids can create strong nucleating peptides among the 10% strongest nucleators in the dataset (Fig. 5c,e). We analyzed the position-specific differences between nucleators and non-nucleators composition and found that the amino acid composition of C-terminal extensions with length 8-11 amino acids (peptides length of 30-33 residues) is similar to that of the 12 amino acid C-terminal extensions (Supp. Fig. 9). However, for C-terminal extensions of length <8 amino acids (peptides length of 24-29 residues), nucleators exhibit a significant enrichment in aromatics at the N-terminus (Fig. 5d and Supp. Fig. 9), revealing that amyloid nucleation is promoted by distinct types of residues depending on peptide length. In ABri-like extensions (i.e. sequences with a Ser at position 23), we find that a C-terminal extension of two specific amino acids, where at least one of them is aliphatic, creates strong nucleators (Fig. 5E).

Discussion

ITM2B/BRI2 mutations affecting its stop codon are associated with familial forms of dementia and deposits containing amyloid forms of the peptides which are generated upon stop-loss have been observed *in vivo*[10,12,27]. Here, we systematically addressed how sequences resulting from stop-loss in *ITM2B/BRI2* can nucleate amyloids using deep and random mutagenesis combined to a selection assay that reports on the amyloid nucleation of thousands of sequences of different length in parallel.

The ADan peptide very rapidly forms amyloids in this cell-based assay, 2-fold faster than Aβ42 for reference, but ABri is at the lower end of the detection capability of our assay. While this sharp difference could be due to limitations in this specific assay, it is in line with results in transgenic mice and drosophila models expressing ABri, which do not exhibit amyloid deposits[28] and feature low neurotoxicity, in contrast with those expressing ADan[27,29].

Thanks to this massively parallel assay, we identify a continuous stretch of residues (L20-F26) in ADan which are crucial for amyloid nucleation and likely constitute the core of ADan amyloids. Surprisingly, changes in hydrophobicity can explain very little of the variance in the ADan dataset (Supp. Fig. 5). It would have been impossible to predict the mutational impact in ADan on the basis of simple physicochemical properties, aggregation predictors or even the latest generation of variant effect predictors[30]. What is more, it would have also been impossible to predict mutational impact in ADan on the basis of the complete mutational landscape of another extracellular amyloid peptide of similar length, Aβ42[21], suggesting that our understanding of the process of amyloid formation by novel peptides is still data limited and highlighting the need of systematically measuring amyloid nucleation for these and other peptides that form amyloids and lead to neurodegeneration[31,32].

By employing unbiased random sequence extension, we expanded the probed sequence space both in terms of length and identity, quantifying amyloid nucleation for ~18,000 sequences. To our knowledge, this is the largest data set of protein sequence extensions currently available. ~32% of them are able to nucleate amyloids. This dataset also reveals that a C-terminal amino acid extension of just two residues is enough to significantly increase the propensity of Bri2 to nucleate amyloids. Other short C-terminal extensions (peptide length < 34 amino acids) also generate strong nucleators. These results are in agreement with a previous study showing that an ADan truncation at position 28 can form beta-sheet rich aggregates *in vitro*[17]. They also suggest that an 'incomplete amyloid motif' exists at the end of the Bri2 sequence, and that specific C-terminal extensions upon stop loss or due to insertions before the stop codon can turn it into an effective driver of amyloid nucleation.

Cryptic amyloid motifs have been discovered in the 3' UTRs of at least three genes that are mutated in neurodegenerative disease[9–11]. Our datasets can now contribute to build better models that can identify and predict more of these motifs. In addition, while stop-codon readthrough of TGA codons happens at a low frequency of 0.01-0.1%[33,34] this phenomenon can be promoted by small molecules[35] such as Gentamicin or ELX-02, which are under clinical trial for the treatment of Herlitz junctional epidermolysis bullosa and Cystic Fibrosis, respectively (clinical trials: NCT04140786 and NCT04135495). Along this line, the possibility of quantifying the impact of C-terminal sequence extensions provides a systematic way to uncover incomplete or hidden amyloids across the genome, gaining the ability to preventively interpreting the impact of stop-codon readthrough on de-novo amyloid formation.

Acknowledgements

Work in the lab of BB is supported by the la Caixa Research Foundation project 'DeepAmyloids' (LCF/PR/HR21/52410004), by the Spanish Ministry of Science, Innovation and Universities (PID2021-127761OB-I00 and RYC2020-028861-I, funded by MCIN/AEI/ 10.13039/501100011033, "ERDF A way of making Europe" and "ESF Investing in your future"). and by the European Union (ERC Consolidator, Glam-MAP, 101125484). Views and opinions expressed are however those of the author(s) only and do not necessarily reflect those of the European Union or the European Research Council. Neither the European Union nor the granting authority can be held responsible for them. IBEC is a member of the CERCA Program /

Generalitat de Catalunya. We thank Ben Lehner and Mike Thompson for discussing the random extension dataset. We thank the Chernoff lab for providing strains and plasmids and the CRG Genomics core technology for sequencing. Figure 1a was created with BioRender.com.

Data availability

Raw sequencing reads and processed nucleation scores are deposited in NCBI's Gene Expression Omnibus (GEO) as GSE244612 and GSE270792. The processed reads and nucleation scores are also available as Supplementary Data 1.

Code availability

All scripts used for downstream analysis and to reproduce all figures are in https://github.com/BEBlab/ADan-BriNNK.

Methods

Library design

The designed libraries contain a total of 1088 unique ADan nucleotide variants (680 single protein variants encoded by 1, 2, and 3 nucleotide changes) and 1088 unique ABri nucleotides variants (680 single protein variants encoded by 1, 2, and 3 nucleotide changes). The random libraries were designed with the sequence encoding for the Bri2 peptide (22 amino acids) at the N-terminus followed by random extensions of 12 amino acids encoded by degenerate codons (NNK, where N = A/C/G/T and K = G/T).

Plasmid Library construction

Libraries were synthesized by Integrated DNA Technologies (IDT) as oligo pools covering the ADan and/or ABri 102 nt sequence or as an ultramer of 12 NNK codons for the random libraries (36 nucleotides), flanked by 25 nt upstream and 21 nt downstream constant regions for cloning. 2 ul of 10uM library pool were extended into a double stranded DNA by a single cycle PCR (Q5 high-fidelity DNA polymerase, NEB) with primers annealing to the constant regions (primers MM_01, Supplementary Data 2). The product was purified from a 2% agarose gel (QIAquick Gel Extraction Kit, Qiagen). In parallel, the pCUP1-Sup35N plasmid was linearized by PCR (Q5 high-fidelity DNA polymerase, NEB; primers MM_02-04, Supplementary Data 2). The product was purified from a 1% agarose gel (QIAquick Gel Extraction Kit, Qiagen). The oligo pool was then ligated into 200 ng of the linearized plasmid in a 1:10 (vector:insert) ratio by a Gibson approach with 3 h of incubation at 50°C followed by dialysis for 3 h on a membrane filter (MF-Millipore 0.025 µm membrane, Merck) and vacuum concentration. The product was transformed into 10-beta Electrocompetent *E. coli* (NEB), by electroporation at 2.0 kV, 200 Ω, 25 µF (BioRad GenePulser machine). For the random libraries, the electroporation was performed three times independently to obtain three random libraries. Cells were recovered in SOC medium for 30 min and grown overnight in 30 ml of LB ampicillin medium. A small amount of cells were also plated in LB ampicillin plates to assess transformation efficiency. A total of >1M transformants were estimated,

337 meaning that each variant in the ADan and ABri libraries are represented ~1000 times. For the
338 three random libraries, ~5M, ~8M and ~2M transformants were obtained, respectively. 5 ml of
339 overnight cultures were harvested to purify the ADan and ABri libraries with a mini prep (QIAprep
340 Miniprep Kit, Qiagen). 50 ml of overnight culture were harvested to purify each random library
341 with a midi prep (Plasmid MIDI Kit, Qiagen).

342 **Yeast transformation**

343 *Saccharomyces cerevisiae* [psi-pin-] (MATα ade1–14 his3 leu2-3,112 lys2 trp1 ura3–52) provided
344 by the Chernoff lab[15] was used in all experiments in this study. Yeast cells were transformed with
345 the ADan and ABri libraries in three biological replicates. Per replicate, an individual colony was
346 grown overnight in 3 ml YPDA medium at 30 °C and 4 g. Cells were diluted in 40 ml to OD600 =
347 0.3 and grown for 4–5 h. When cells reached the exponential phase (OD~0.8–0.9) cells were
348 harvested at 3000 × g for 5 min, washed with 50 ml milliQ, centrifuged at 3000 × g for 5 min and
349 washed with 25 ml SORB buffer (100 mM LiOAc, 10 mM Tris pH 8.0, 1 mM EDTA, 1 M sorbitol).
350 Cells were resuspended in 1.4 ml of SORB and incubated 30 min on an orbital shaker. After
351 incubation, 800 ng of library and 30 ul of ssDNA (UltraPure, Thermo Scientific) were added and
352 incubated for 5 min at room temperature and then 10 min on an orbital shaker. 6 ml of YTB-PEG
353 (100 mM LiOAc, 10 mM Tris pH 8.0, 1 mM EDTA, 40% PEG 3350) and 580 ul of DMSO were
354 added to the cells. Heat-shock was performed at 42 °C for 20 min in a liquid bath with intermittent
355 shaking. Cells were harvested and incubated in 50 ml of recovery medium (YPDA medium +
356 Sorbitol 0.5 M) for 1 h at 30 °C. Cells were harvested and grown in 50 ml plasmid selection
357 medium (-URA, 2% glucose) for 50 h at 30 °C. A small amount of cells were also plated in plasmid
358 selection solid medium to assess transformation efficiency. 60,000-100,000 transformants were
359 estimated for each biological replicate, meaning that each variant in the library is represented at
360 least 50 times. After 50 h, cells were diluted in 50 ml plasmid selection medium to OD= 0.05 and
361 grown exponentially for 15 h. Finally, the culture was harvested and stored at −80 °C in 25 %
362 glycerol.

363 **Large-scale yeast transformation of random libraries**

364 Yeast cells were transformed with the plasmid random libraries midi prep in three independent
365 experiments. For each of the experiments, an overnight pre-growth culture in 25 ml of YPDA
366 medium at 30˚C was diluted to OD600 = 0.3 in 175 ml YPDA and incubated at 30˚C 200 rpm for
367 ~4 hr. When cells reached the exponential phase, they were harvested, washed with milliQ, and
368 resuspended in sorbitol mixture (100 mM LiOAc, 10 mM Tris pH 8, 1 mM EDTA, 1M sorbitol).
369 After a 30 min incubation at room temperature (RT), 4 ug of plasmid library and 175 µl of ssDNA
370 (UltraPure, Thermo Scientific) were added to the cells. YTB-PEG mixture (100 mM LiOAc, 10 mM
371 Tris pH 8, 1 mM EDTA pH 8, 40% PEG3350) was also added and cells were incubated for 30 min
372 at RT and heat-shocked for 15 min at 42˚C in a water bath. Cells were harvested, washed,
373 resuspended in 250 ml recovery medium (YPD, sorbitol 0.5M, 70 mg/L adenine) and incubated
374 for 1 hr at 30˚C 200 rpm. After recovery, cells were resuspended in 350 ml -URA plasmid selection
375 medium and allowed to grow for 50 hr. Transformation efficiency was calculated for each tube of
376 transformation by plating an aliquot of cells in -URA plates. Each of the three random libraries
377 was bottlenecked to ~500,000 yeast transformants. Two days after transformation, the culture

378 was diluted to OD600 = 0.08 in 500 ml -URA medium and grown until exponential phase. At this
379 stage, cells were harvested and stored at -80˚C in 25% glycerol.

380 **Selection experiments**

381 *In vivo* selection assays were performed in three independent biological replicates for ADan and
382 ABri libraries. For each replicate, cells were thawed from −80 °C in 50 ml plasmid selection
383 medium at OD = 0.05 and grown until exponential for 15 h. At this stage, cells were harvested
384 and resuspended in 50 ml protein induction medium (-URA, 2% glucose, 100 μM Cu_2SO_4) at OD
385 = 0.1. After 24 h the 40 ml input pellets were collected, and cells were plated on -ADE-URA
386 selection medium in 145-cm2 plates (Nunc, Thermo Scientific). Plates were incubated at 30 °C
387 for 7 days. Finally, colonies were scraped off the plates with PBS 1x and harvested by
388 centrifugation to collect the output pellets. Both input and output pellets were stored at −20 °C
389 before DNA extraction. Three input and three output samples were processed for
390 sequencing. For each of the three random libraries, one selection experiment was performed,
391 and one input sample and three technical replicates of the output pellet were processed for
392 sequencing as described above.

393 **DNA extraction and sequencing library preparation**

394 Input and output pellets were resuspended in 0.5ml extraction buffer (2% Triton-X, 1% SDS, 100
395 mM NaCl, 10 mM Tris-HCl pH 8, 1 mM EDTA pH 8). They were then frozen for 10 min in an
396 ethanol-dry ice bath and heated for 10 min at 62 °C. This cycle was repeated twice. 0.5ml of
397 phenol:chloroform:isoamyl (25:24:1 mixture, Thermo Scientific) was added together with glass
398 beads (Sigma). Samples were vortexed for 10 min and centrifuged for 30 min at 2000 × g. The
399 aqueous phase was then transferred to a new tube, and mixed again with
400 phenol:chloroform:isoamyl, vortexed and centrifuged for 45 min at 2000 × g. Next, the aqueous
401 phase was transferred to another tube with 1:10 V 3 M NaOAc and 2.2 V cold ethanol 96% for
402 DNA precipitation. After 30 min at −20 °C, samples were centrifuged and pellets were dried
403 overnight. The following day, pellets were resuspended in 0.3 ml TE 1X buffer and treated with
404 10 μl RNAse A (Thermo Scientific) for 30 min at 37 °C. DNA was finally purified using 10 μl of
405 silica beads (QIAEX II Gel Extraction Kit, Qiagen) and eluted in 30 μl elution buffer. Plasmid
406 concentrations were measured by quantitative PCR with SYBR green (Merck) and primers
407 annealing to the origin of replication site of the PCUP1-Sup35N plasmid at 58 °C for 40 cycles
408 (primers MM_05-06, Supplementary Data 2). The library for high-throughput sequencing was
409 prepared in a two-step PCR (Q5 high-fidelity DNA polymerase, NEB). In PCR1, 50 million of
410 molecules (ADan and ABri libraries) or 300 million molecules (random libraries) were amplified
411 for 15 cycles with frame-shifted primers with homology to Illumina sequencing primers (primers
412 MM_07–26, Supplementary Data 2). The products were treated with ExoSAP treatment
413 (Affymetrix) and purified by column purification (MinElute PCR Purification Kit, Qiagen). They
414 were then amplified for 12 cycles in PCR2 with Illumina-indexed primers (primers MM_27–67,
415 Supplementary Data 2). For ADan and ABri libraries, the six samples (one input-output pair per
416 biological replicate) were pooled together equimolarly and the final product was purified from a
417 2% agarose gel with 20 μl silica beads (QIAEX II Gel Extraction Kit, Qiagen). The three random
418 libraries were purified individually. The libraries were sent for 125 bp paired-end sequencing in an

419 Illumina HiSeq2500 sequencer at the CRG Genomics core facility. In total, >10 million paired-end
420 reads were obtained for each of ADan and ABri libraries, representing >1000x read coverage.
421 Each of the random libraries obtained >45 million paired-end reads.

422 **Individual variant testing**

423 Selected variants, from ADan and ABri libraries, for individual testing were obtained by PCR
424 linearisation (Q5 high-fidelity DNA polymerase, NEB) with mutagenic primers (primers MM_68-
425 85, Supplementary Data 2) or by ultramer amplification and Gibson assembly with the linearized
426 plasmid for the sequences coming from the random libraries (primers MM_86-91). PCR products
427 were treated with Dpn1 overnight and transformed in DH5α competent *E. coli*. Plasmids were
428 purified by miniprep (QIAprep Miniprep Kit, Qiagen) and transformed into yeast cells. All mutated
429 plasmids were verified by Sanger sequencing. For measuring growth in selective conditions, yeast
430 cells expressing individual variants were grown overnight in a plasmid selection medium (-URA
431 2% glucose). They were then diluted to OD 0.1 in protein induction medium (-URA 2% glucose
432 100 μM Cu_2SO_4) and grown for 24 h. Cells were plated on -URA (control) and -ADE-URA
433 (selection) plates in three independent replicates and allowed to grow for 7 days at 30 °C. Adenine
434 growth was calculated as the percentage of colonies in -ADE-URA relative to colonies in -URA.

435 For individual growth rate measurements, yeast cells expressing individual variants were grown
436 overnight in plasmid selection medium (-URA 2% glucose) and diluted to OD 0.2 until exponential.
437 They were then diluted again to OD 0.1 in non-inducing (-URA 2% glucose) and inducing (-URA
438 2% glucose 100 μM Cu_2SO_4) protein expression mediums. Cell growth was measured at 30 °C
439 for >48 h at 10 min intervals in a microplate reader (Spark, Tecan) in three biological replicates.
440 Growth rates were calculated using the GrowthCurver package in R.

441 **Data processing**

442 FastQ files from paired end sequencing of the libraries were processed using DiMSum
443 (https://github.com/lehner-lab/DiMSum)[36], an R pipeline for analyzing deep mutational scanning
444 data. 5′ and 3′ constant regions were trimmed, allowing a maximum of 20% of mismatches relative
445 to the reference sequence. Sequences with a Phred base quality score below 30 were discarded.
446 Non-designed variants were also discarded for further analysis, as well as variants with fewer
447 than 100 (random libraries) or 200 (ADan and ABri libraries) input reads in all of the replicates.

448 **Nucleation scores and error estimates**

449 The DiMSum package (https://github.com/lehner-lab/DiMSum)[36] was also used to calculate
450 nucleation scores (NS) and their error estimates for each variant in each biological replicate as:

451 $$\text{Nucleation score} = ESi - ESwt$$

452 Where ESi = log(Fi OUTPUT) - log(Fi INPUT) for a specific variant and ESwt = log(Fwt OUTPUT)
453 - log(Fwt INPUT) for ADan or ABri WT.

454 NSs for each variant were merged across biological replicates using error-weighted mean and
455 centered to the WT NS. All NS and associated error estimates are available in Supplementary
456 Data 1.

457 The ADan library has a good signal/noise ratio due to its significant growth in the selection assay.
458 After NSs centering, each variant was tested against the WT NS at FDR=0.1 and classified in
459 three possible groups: WT-like, NS_inc and NS_dec. Sigma values were normalized to the
460 interquartile range and WT-like variants with a normalized sigma value above a cut-off of 0.2 were
461 excluded. The same procedure was part of ABri library processing. As this library has a poor
462 signal/noise ratio (Supp. Fig. 2a), few variants passed the filtering process. NS was obtained for
463 676 unique ADan variants and 679 unique ABri variants. 664 confident estimates (with low
464 normalized sigma value) were obtained for the ADan library and 177 in the ABri library.

465 For the random extensions libraries, 1 input and 3 output sequencing results were used. DimSum
466 was run using an arbitrary WT sequence chosen among those with high input counts. The
467 sequences used were: TTGTAGGTTGCTCAGGAGGTTAATACGTATACGTAG,
468 TTTTGTTAGTTTGATGTGCATGAGTGTCTGTAGTGT and
469 TGGAAGGGGACGATGGTTGTGGGTAGTAATTGGCCG for experiment 1, 2 and 3,
470 respectively.

471 NSs for each sequence were merged within each replicate using error-weighted mean and
472 centered to the mode value of the distribution (as most of the sequences do not nucleate). Those
473 sequences that are present in the input and not in the output were imputed with the mode value
474 of the distribution. Most of the sequences have a nucleation score of 0. Consequently, we
475 classified sequences with a nucleation score significantly (FDR=0.05) greater than 0 as
476 nucleators and all other sequences as non-nucleators. Duplicated sequences were merged and
477 mean nucleation score and the mode of the nucleator status was calculated. We discarded those
478 non-nucleators sequences that had big errors and a mean nucleation score above the minimum
479 nucleator score. For each of the random libraries we classified the top 10% nucleator sequences
480 as another group. Finally, variants from the three experiments were merged and duplicated
481 variants were treated as previously described. 17,952 unique sequences with NS were obtained
482 (7,783 experiment 1; 5,562 experiment 2 and 4,607 experiment 3). All NS estimates are available
483 in Supplementary Data 1.

484 **Aggregation predictors**

485 For the aggregation predictors (Tango, Amypred, Camsol, Aggrescan)[37–40] scores were calculated
486 per sequence and, if necessary, individual residue level scores were summed to obtain a score
487 per single AA mutation sequence. We also used the Kyte-Doolittle hydrophobicity scale[41].

488 **Statistics and reproducibility**

489 Based on the transformation efficiency, each variant in the designed libraries (n = 1088 nucleotide
490 variants each) is expected to be represented at least 10x at each step-in selection experiments
491 and library preparation. In terms of sequencing, reads that did not pass the QC filters using the

492 DiMSum package were excluded (https://github.com/lehner-lab/DiMSum)[36]. The experiments
493 were not randomized. The Investigators were not blinded to allocation during experiments and
494 outcome assessment.

495

496

497

498 ## References

499 1. Hamby, S. E., Thomas, N. S., Cooper, D. N. & Chuzhanova, N. A meta-analysis of single
500 base-pair substitutions in translational termination codons ('nonstop' mutations) that
501 cause human inherited disease. *Hum Genomics* **5**, 241 (2011).
502 2. Monaghan, L., Longman, D. & Cáceres, J. F. Translation-coupled mRNA quality control
503 mechanisms. *EMBO J* (2023) doi:10.15252/embj.2023114378.
504 3. Kramarski, L. & Arbely, E. Translational read-through promotes aggregation and shapes
505 stop codon identity. *Nucleic Acids Res* **48**, 3747–3760 (2020).
506 4. Arribere, J. A. *et al.* Translation readthrough mitigation. *Nature* **534**, 719–723 (2016).
507 5. Dhamija, S. *et al.* A pan-cancer analysis reveals nonstop extension mutations causing
508 SMAD4 tumour suppressor degradation. *Nat Cell Biol* **22**, 999–1010 (2020).
509 6. Shibata, N. *et al.* Degradation of Stop Codon Read-through Mutant Proteins via the
510 Ubiquitin-Proteasome System Causes Hereditary Disorders. *Journal of Biological*
511 *Chemistry* **290**, 28428–28437 (2015).
512 7. Sun, J. *et al.* Functional analysis of a nonstop mutation in MITF gene identified in a
513 patient with Waardenburg syndrome type 2. *J Hum Genet* **62**, 703–709 (2017).
514 8. Hollingsworth, T. J. & Gross, A. K. The Severe Autosomal Dominant Retinitis Pigmentosa
515 Rhodopsin Mutant Ter349Glu Mislocalizes and Induces Rapid Rod Cell Death. *Journal of*
516 *Biological Chemistry* **288**, 29047–29055 (2013).
517 9. Rebelo, A. P. *et al.* Cryptic Amyloidogenic Elements in the 3′ UTRs of Neurofilament
518 Genes Trigger Axonal Neuropathy. *The American Journal of Human Genetics* **98**, 597–
519 614 (2016).
520 10. Vidal, R. *et al.* A stop-codon mutation in the BRI gene associated with familial British
521 dementia. *Nature* **399**, 776–781 (1999).
522 11. Bock, A. S. *et al.* A nonstop variant in *REEP1* causes peripheral neuropathy by
523 unmasking a 3′UTR-encoded, aggregation-inducing motif. *Hum Mutat* **39**, 193–196
524 (2018).
525 12. Vidal, R. *et al.* A decamer duplication in the 3′ region of the *BRI* gene originates an
526 amyloid peptide that is associated with dementia in a Danish kindred. *Proceedings of the*
527 *National Academy of Sciences* **97**, 4920–4925 (2000).
528 13. Rhyu, J.-M. *et al.* A Novel c.800G>C Variant of the ITM2B Gene in Familial Korean
529 Dementia. *Journal of Alzheimer's Disease* **93**, 403–409 (2023).
530 14. Liu, X. *et al.* A Novel ITM2B Mutation Associated with Familial Chinese Dementia.
531 *Journal of Alzheimer's Disease* **81**, 499–505 (2021).
532 15. Chandramowlishwaran, P. *et al.* Mammalian amyloidogenic proteins promote prion
533 nucleation in yeast. *Journal of Biological Chemistry* **293**, 3436–3450 (2018).
534 16. Seuma, M., Faure, A. J., Badia, M., Lehner, B. & Bolognesi, B. The genetic landscape for
535 amyloid beta fibril nucleation accurately discriminates familial Alzheimer's disease
536 mutations. *Elife* **10**, (2021).
537 17. Todd, K., Ghiso, J. & Rostagno, A. Oxidative stress and mitochondria-mediated cell death
538 mechanisms triggered by the familial Danish dementia ADan amyloid. *Neurobiol Dis* **85**,
539 130–143 (2016).

18. Rousseau, F., Schymkowitz, J. & Serrano, L. Protein aggregation and amyloidosis: confusion of the kinds? *Curr Opin Struct Biol* **16**, 118–126 (2006).
19. Bhoite, S. S., Kolli, D., Gomulinski, M. A. & Chapman, M. R. Electrostatic interactions mediate the nucleation and growth of a bacterial functional amyloid. *Front Mol Biosci* **10**, (2023).
20. Sant'Anna, R. *et al.* The Importance of a Gatekeeper Residue on the Aggregation of Transthyretin. *Journal of Biological Chemistry* **289**, 28324–28337 (2014).
21. Seuma, M., Lehner, B. & Bolognesi, B. An atlas of amyloid aggregation: the impact of substitutions, insertions, deletions and truncations on amyloid beta fibril nucleation. *Nat Commun* **13**, 7084 (2022).
22. Chen, S. *et al.* A genomic mutational constraint map using variation in 76,156 human genomes. *Nature* **625**, 92–100 (2024).
23. Holton, J. L. *et al.* Regional Distribution of Amyloid-Bri Deposition and Its Association with Neurofibrillary Degeneration in Familial British Dementia. *Am J Pathol* **158**, 515–526 (2001).
24. Ghiso, J. A. *et al.* Systemic Amyloid Deposits in Familial British Dementia. *Journal of Biological Chemistry* **276**, 43909–43914 (2001).
25. Lashley, T. *et al.* Molecular chaperons, amyloid and preamyloid lesions in the BRI2 gene-related dementias: a morphological study. *Neuropathol Appl Neurobiol* **32**, 492–504 (2006).
26. Madeira, F. *et al.* Search and sequence analysis tools services from EMBL-EBI in 2022. *Nucleic Acids Res* **50**, W276–W279 (2022).
27. Vidal, R., Barbeito, A. G., Miravalle, L. & Ghetti, B. Cerebral Amyloid Angiopathy and Parenchymal Amyloid Deposition in Transgenic Mice Expressing the Danish Mutant Form of Human BRI $_2$. *Brain Pathology* **19**, 58–68 (2009).
28. Pickford, F., Coomaraswamy, J., Jucker, M. & McGowan, E. Modeling Familial British Dementia in Transgenic Mice. *Brain Pathology* **16**, 80–85 (2006).
29. Marcora, M. S. *et al.* Amyloid peptides ABri and ADan show differential neurotoxicity in transgenic Drosophila models of familial British and Danish dementia. *Mol Neurodegener* **9**, 5 (2014).
30. Livesey, B. J. & Marsh, J. A. Interpreting protein variant effects with computational predictors and deep mutational scanning. *Dis Model Mech* **15**, (2022).
31. Seuma, M. & Bolognesi, B. Understanding and evolving prions by yeast multiplexed assays. *Curr Opin Genet Dev* **75**, 101941 (2022).
32. Thompson, M. *et al.* Interpretably deep learning amyloid nucleation by massive experimental quantification of random sequences. *bioRxiv* 2024.07.13.603366 (2024) doi:10.1101/2024.07.13.603366.
33. Floquet, C., Hatin, I., Rousset, J.-P. & Bidou, L. Statistical Analysis of Readthrough Levels for Nonsense Mutations in Mammalian Cells Reveals a Major Determinant of Response to Gentamicin. *PLoS Genet* **8**, e1002608 (2012).
34. Dabrowski, M., Bukowy-Bieryllo, Z. & Zietkiewicz, E. Translational readthrough potential of natural termination codons in eucaryotes – The impact of RNA sequence. *RNA Biol* **12**, 950–958 (2015).

583 35. Toledano, I., Supek, F. & Lehner, B. Genome-scale quantification and prediction of
584 pathogenic stop codon readthrough by small molecules. *bioRxiv* 2023.08.07.552350
585 (2023) doi:10.1101/2023.08.07.552350.
586 36. Faure, A. J., Schmiedel, J. M., Baeza-Centurion, P. & Lehner, B. DiMSum: an error
587 model and pipeline for analyzing deep mutational scanning data and diagnosing common
588 experimental pathologies. *Genome Biol* **21**, 207 (2020).
589 37. Fernandez-Escamilla, A.-M., Rousseau, F., Schymkowitz, J. & Serrano, L. Prediction of
590 sequence-dependent and mutational effects on the aggregation of peptides and proteins.
591 *Nat Biotechnol* **22**, 1302–1306 (2004).
592 38. Charoenkwan, P. *et al.* AMYPred-FRL is a novel approach for accurate prediction of
593 amyloid proteins by using feature representation learning. *Sci Rep* **12**, 7697 (2022).
594 39. Sormanni, P., Aprile, F. A. & Vendruscolo, M. The CamSol Method of Rational Design of
595 Protein Mutants with Enhanced Solubility. *J Mol Biol* **427**, 478–490 (2015).
596 40. Conchillo-Solé, O. *et al.* AGGRESCAN: a server for the prediction and evaluation of 'hot
597 spots' of aggregation in polypeptides. *BMC Bioinformatics* **8**, 65 (2007).
598 41. Kyte, J. & Doolittle, R. F. A simple method for displaying the hydropathic character of a
599 protein. *J Mol Biol* **157**, 105–132 (1982).
600 42. Kanehisa, M. I. & Tsong, T. Y. Local hydrophobicity stabilizes secondary structures in
601 proteins. *Biopolymers* **19**, 1617–1628 (1980).

602

603

604

605

606

607

608

609

610

611

612

613

614

615

616 ## Figures Legends

617 **Figure 1. ADan and its truncations are strong nucleators. A.** Schematics of ITMB2/BRI2
618 cleavage by the furin protease. **B.** Schematics of *ITMB2/BRI2* and dementia-related mutations at
619 the nucleotide and protein level. cDNA coordinates are detailed at the top and stop codons
620 (conventional or alternative) are represented with bold fonts and upper case. The exon and its
621 translated protein product is highlighted in purple. Extended products resulting from mutations are
622 highlighted in yellow (ABri and ABri-like) and orange (ADan). Familial dementia mutations are
623 detailed over the arrows. **C.** Relative growth of cells expressing Bri2, ABri or ADan fusions
624 calculated as number of colonies growing in the selective conditions of the amyloid nucleation
625 assay (-URA, –Ade) over colonies growing in the absence of selection (-URA)[15]. Error bars
626 indicate the standard deviation of the experiments (n=3). **D.** Deep mutagenesis scheme. A library
627 of sequences of interest is expressed in yeast and selected for amyloid nucleation as reported in
628 Seuma *et al*.[16]. Amyloid nucleation scores are obtained through deep sequencing of input and
629 output samples. **E.** Correlation of nucleation scores between two biological replicates for variants
630 in the ADan library. Pearson correlation coefficient and p-value are indicated. **F.** Correlation
631 between nucleation scores obtained from selection and deep sequencing with relative growth of
632 individual variants in selective over non-selective conditions (n=5). Vertical and horizontal error
633 bars indicate estimated sigma errors and standard deviation of the experiments (n=3),
634 respectively. Pearson correlation coefficient and p-values are indicated. **G.** Distribution of
635 nucleation scores for each class of mutations in ADan library. **H.** ADan truncations nucleation
636 propensity. The horizontal line indicates the weighted mean nucleation score of Bri2 truncations
637 (up to position 22). Vertical error bars indicate 95% confidence interval of the mean.

638 **Figure 2. Deep mutagenesis of ADan. A.** Frequency of variants increasing or decreasing
639 nucleation at FDR=0.1 and variants that are WT-like. **B.** Heatmap of nucleation scores for ADan
640 single amino acid substitutions. The WT amino acid and position are indicated in the x-axis and
641 the mutant amino acid is indicated in the y-axis. Synonymous variants are indicated as "ADan",
642 missense variants due to SNVs are indicated with "\" and SNVs present in GnomAD with a "\\" in
643 the upper right corner of the cell. The distribution of nucleation scores for each position is
644 summarized in the violin plots below the heatmap. The number of variants increasing or
645 decreasing nucleation at FDR=0.1 per position are indicated as stack bars at the bottom. The
646 distribution of nucleation scores for each mutation is summarized in the violin plots at the right-
647 hand side of the heatmap. The number of variants increasing or decreasing nucleation at
648 FDR=0.1 per mutation are indicated as stack bars at the right. **C.** Frequency of single amino acid
649 substitutions that are increasing or decreasing nucleation (FDR=0.1) upon substituting specific
650 WT amino acid.

651 **Figure 3. Comparing the mutational effects of single AA variants in ADan, Aβ42 and ABri**
652 **libraries. A-B.** Correlation of average nucleation scores for each type of substitution of the same
653 amino acid (**A**) or to the same amino acid (**B**) in ADan and Aβ42. **C-D.** Correlation of average
654 nucleation scores for each substitution to the same amino acid (**C**) or of the same amino acid (**D**)
655 in ADan and ABri. **E.** Correlation of ADan and ABri nucleation scores for positions where more

656 than 4 ABri variants were measured. ADan residues are detailed in orange and ABri residues in
657 red. Pearson correlation coefficient and p-value are indicated in each plot.

658 **Figure 4. Amyloid nucleation by Bri2 random extensions of 12 amino acids. A.** Random
659 extensions design and sequence space. A library of random sequences encoded by 12
660 degenerated NNK codons was expressed in yeast and selected for amyloid nucleation. **B.**
661 Nucleation scores distribution of random sequences present in replicate 1. Variants are classified
662 as non-nucleators (red), nucleators (blue) or top 10% nucleators (dark blue). **C.** Correlation
663 between nucleation scores obtained from selection and deep sequencing with relative growth of
664 individual variants in selective over non-selective conditions (n=6). Pearson correlation coefficient
665 and p-values are indicated. **D.** Hydrophobicity (Kyte-Doolitle[41]) and beta-sheet propensity
666 (Kanehisa-Tsong[42]) of assayed sequences relative to human proteome. **E.** The percent
667 composition of residues grouped by their physicochemical properties in nucleators and non-
668 nucleators sequences. **F.** Heatmap of normalized frequencies for Bri2 random extensions. The
669 distribution of normalized frequencies for each position is summarized in the violin plots below
670 the heatmap and the distribution of normalized frequencies for each mutation is summarized in
671 the violin plots at the right-hand side of the heatmap. **G.** The position-specific differences in amino
672 acid type frequencies across nucleating and non-nucleating sequences. Asterisks indicate
673 marginal p-value (chi-square test). $p<0.05$: *; $p<0.01$: **; $p<0.001$: ***.

674 **Figure 5. Nucleators resulting from Bri2 random extensions of different lengths have**
675 **different specific amino acid enrichment. A.** Range of lengths for the Bri2 random extensions
676 measured in the assay. **B.** Percentage of non-nucleators, nucleators and top 10% nucleators
677 sequences for each peptide length. **C.** Nucleation scores distribution of random extended
678 sequences present in replicate 1. The length of the peptide is indicated inside the grey box of
679 each plot. Variants are classified as non-nucleators (red), nucleators (blue) or top 10% nucleators
680 (dark blue). **D.** The position-specific differences in aromatic amino acids frequencies across
681 nucleating and non-nucleating sequences in truncations of different length. The length of the
682 peptide is indicated inside the grey box of each plot. Asterisks indicate marginal p-value (chi-
683 square test). $p<0.05$: *; $p<0.01$: **; $p<0.001$: ***. **E.** Top nucleating sequences of ADan-like
684 extensions (top) and ABri-like extensions (bottom) of 2 amino acids. Bri2 sequence is highlighted
685 in purple and the extended sequence in green.

686 **Supplementary Figure 1. ADan and ABri nucleation. A.** Schematics of the reporter assay. **B.**
687 Individual testing of SupN (negative control), Aβ42 (positive control), Bri2, ABri and ADan in the
688 reporter assay. Relative growth of cells expressing each sequence, calculated as the number of
689 colonies growing in the selective conditions of the amyloid nucleation assay (-URA, –Ade) over
690 colonies growing in the absence of selection (-URA). t-test significance is indicated (n=3 biological
691 replicates/variant). **C.** Individually measured growth rates for Bri2, ABri and ADan, in non-inducing
692 (no Cu^{2+}) and inducing (Cu^{2+}) protein expression conditions (n=3 biological replicates/variant).
693 One-way ANOVA with Dunnett's multiple comparisons test against Bri2 Cu^{2+}. **D.** Correlation of
694 nucleation scores between biological replicates for variants in the ADan library. Pearson
695 correlation coefficient and p-value are indicated.

696 **Supplementary Figure 2. Deep mutagenesis of ABri. A.** Normalized sigma distribution for
697 variants increasing, decreasing or not affecting nucleation at FDR=0.1. Vertical line indicates
698 threshold value for considering low sigma. **A.** Correlation of nucleation scores between two
699 biological replicates for variants in the ABri library. Pearson correlation coefficient and p-value are
700 indicated. **B.** Correlation of nucleation scores obtained from selection and deep sequencing with
701 relative growth of individual variants in selective conditions (n=5). Vertical and horizontal error
702 bars indicate estimated sigma errors and standard deviation of the experiments (n=3),
703 respectively. Pearson correlation coefficient and p-values are indicated. **C.** Correlation of
704 nucleation scores between biological replicates for variants in the ABri library. Pearson correlation
705 coefficient and p-value are indicated. **D.** Heatmap of nucleation scores for ABri single amino acid
706 substitutions. The WT amino acid and position are indicated in the x-axis and the mutant amino
707 acid is indicated in the y-axis. Synonymous variants are indicated as "ABri", missense variants
708 due to SNVs are indicated with "\" and SNVs present in GnomAD with a "\\" in the upper right
709 corner of the cell. Missing variants have been excluded on the basis of poor sequencing quality
710 and low normalized sigma values (see Methods).

711 **Supplementary Figure 3. Mutational effects of single AA substitutions.** Heatmap of FDR
712 categories for the effects of single amino acid substitutions. The WT amino acid and position are
713 indicated in the x-axis and the mutant amino acid is indicated in the y-axis. Synonymous mutants
714 are indicated with "ADan" (**A**) or "ABri" (**B**). Missense variants due to SNVs present in GnomAD
715 are indicated with "\" in the upper right corner of the cell. The number of variants increasing or
716 decreasing nucleation at different FDRs per position are indicated as stack bars at the bottom.

717 **Supplementary Figure 4. Comparing the mutational effects of single amino acid variants**
718 **in ADan, Aβ42 and ABri libraries.** Correlation of nucleation scores between ADan and Aβ42
719 aligned at N-term (**A**), at C-term (**B**) and with ClustalO (**C**), and between ADan and ABri (**D**).

720 **Supplementary Figure 5. Physicochemical features partially explain nucleation. A.** ADan
721 nucleation scores correlation with amyloid propensity predictors (Tango and Amypred), solubility
722 predictors (CamSol) and Kyte-Doolittle hydrophobicity score. Red dots indicate the values for the
723 WT sequence. Pearson correlation coefficient and p-values are indicated. **B.** Nucleation score
724 distributions arranged by the number of charged residues (y-axis) and the total net charge (x-axis)
725 in ADan. Numbers inside each cell indicate the number of positive and negative residues. The
726 horizontal line indicates WT nucleation score (0).

727 **Supplementary Figure 6. Bri2 random extensions. A.** Distribution of nucleation scores for
728 random sequences of length 34 for replicates 2 and 3. Variants are classified as non-nucleators
729 (red), nucleators (blue) or top 10% nucleators (dark blue). **B.** Nucleation scores distribution of
730 random sequences present in replicate 2 and 3 (top and bottom, respectively). The length of the
731 peptide is indicated inside the grey box of each plot. Variants are classified as non-nucleators
732 (red), nucleators (blue) or top 10% nucleators (dark blue). **C.** The position-specific differences in
733 amino acid frequencies of sequences 34 amino acid long, across nucleating and non-nucleating
734 sequences. Asterisks indicate marginal p-value (chi-square test). $p<0.05$: *; $p<0.01$: **; $p<0.001$:
735 ***.

736 **Supplementary Figure 7. ABri-like random dataset. A.** Nucleation scores distribution of
737 random sequences present in the three replicates. Variants are classified as non-nucleators (red),
738 nucleators (blue) or top 10 nucleators (dark blue). **B.** Heatmap of normalized frequencies for ABri-
739 like random extensions. The distribution of normalized frequencies for each position is
740 summarized in the violin plots below the heatmap and the distribution of normalized frequencies
741 for each mutation is summarized in the violin plots at the right-hand side of the heatmap. **C.** The
742 position-specific differences in amino acid type frequencies across nucleating and non-nucleating
743 sequences. Asterisks indicate marginal p-value (chi-square test). $p<0.05$: *; $p<0.01$: **; $p<0.001$:
744 ***.

745 **Supplementary Figure 8. Performance of amyloid predictors on Bri2 random extension**
746 **dataset.** ROC curves of state-of-the-art amyloid predictors on non-nucleators vs nucleators (**A**)
747 and non-nucleators vs top 10% nucleators sequences (**B**). AUC and confidence interval is
748 detailed for each of the predictors.

749 **Supplementary Figure 9. Position-specific differences in amino acid type frequencies for**
750 **truncated sequences across nucleating and non-nucleating sequences.** Asterisks indicate
751 marginal p-value (chi-square test). $p<0.05$: *; $p<0.01$: **; $p<0.001$: ***.

Figure 1

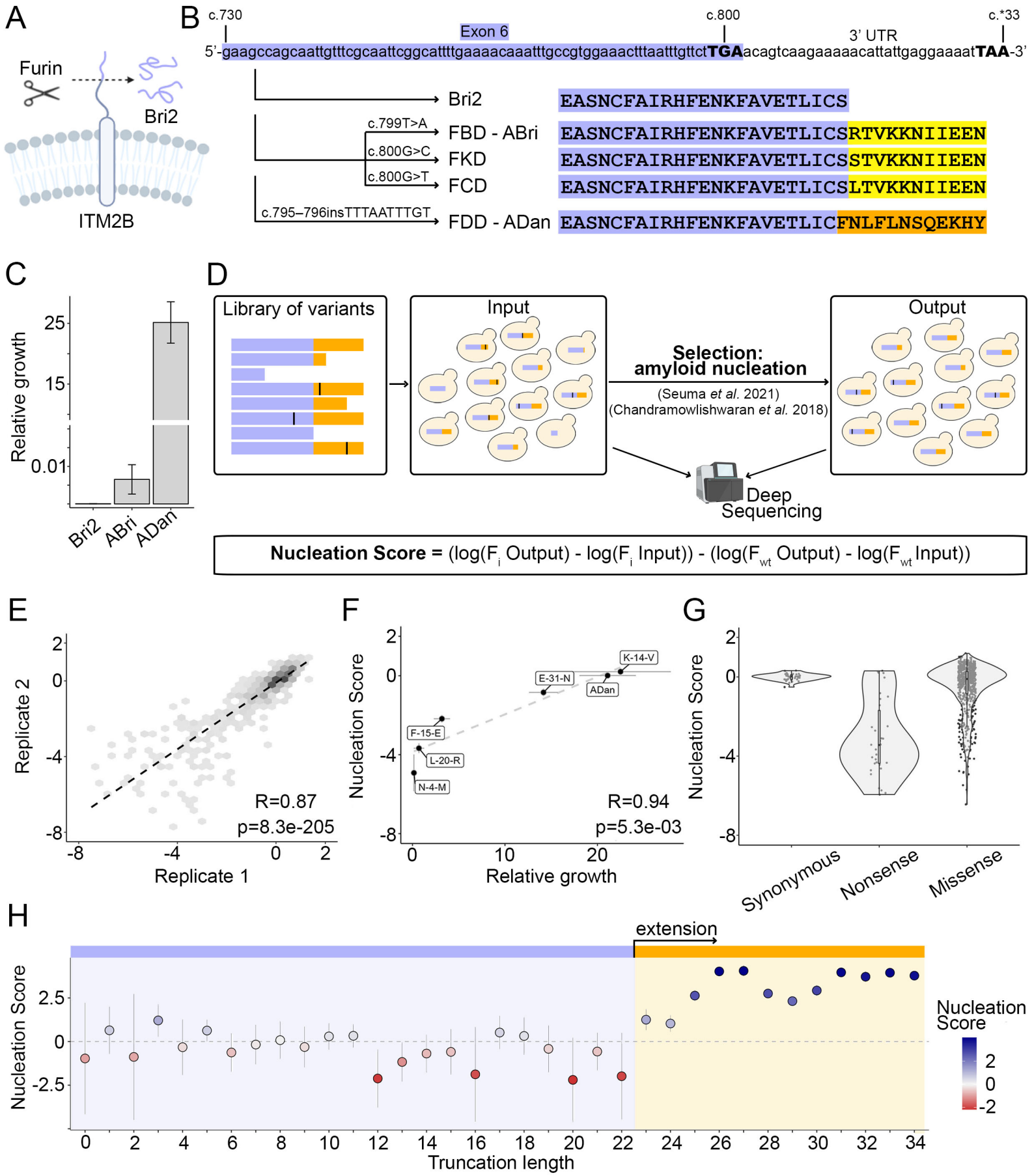
A
Furin
Bri2
ITM2B
B
c.730
Exon 6
c.800
3' UTR
c.*33
5'-gaagccagcaattgtttcgcaattcggcattttgaaaacaaatttgccgtggaaactttaatttgttctTGAacagtcaagaaaaacattattgaggaaaatTAA-3'
Bri2
EASNCFAIRHFENKFAVETLICS
c.799T>A
FBD - ABri
EASNCFAIRHFENKFAVETLICSRTVKKNIIEEN
c.800G>C
FKD
EASNCFAIRHFENKFAVETLICSSTVKKNIIEEN
c.800G>T
FCD
EASNCFAIRHFENKFAVETLICSLTVKKNIIEEN
c.795–796insTTTAATTTGT
FDD - ADan
EASNCFAIRHFENKFAVETLICFNLFLNSQEKHY
C
Relative growth
25
15
0.01
Bri2
ABri
ADan
D
Library of variants
Input
Selection:
amyloid nucleation
(Seuma et al. 2021)
(Chandramowlishwaran et al. 2018)
Output
Deep
Sequencing
Nucleation Score = (log(F_i Output) - log(F_i Input)) - (log(F_wt Output) - log(F_wt Input))
E
Replicate 2
Replicate 1
R=0.87
p=8.3e-205
F
Nucleation Score
Relative growth
K-14-V
E-31-N
ADan
F-15-E
L-20-R
N-4-M
R=0.94
p=5.3e-03
G
Nucleation Score
Synonymous
Nonsense
Missense
H
extension
Nucleation Score
Truncation length
Nucleation
Score

Figure 2

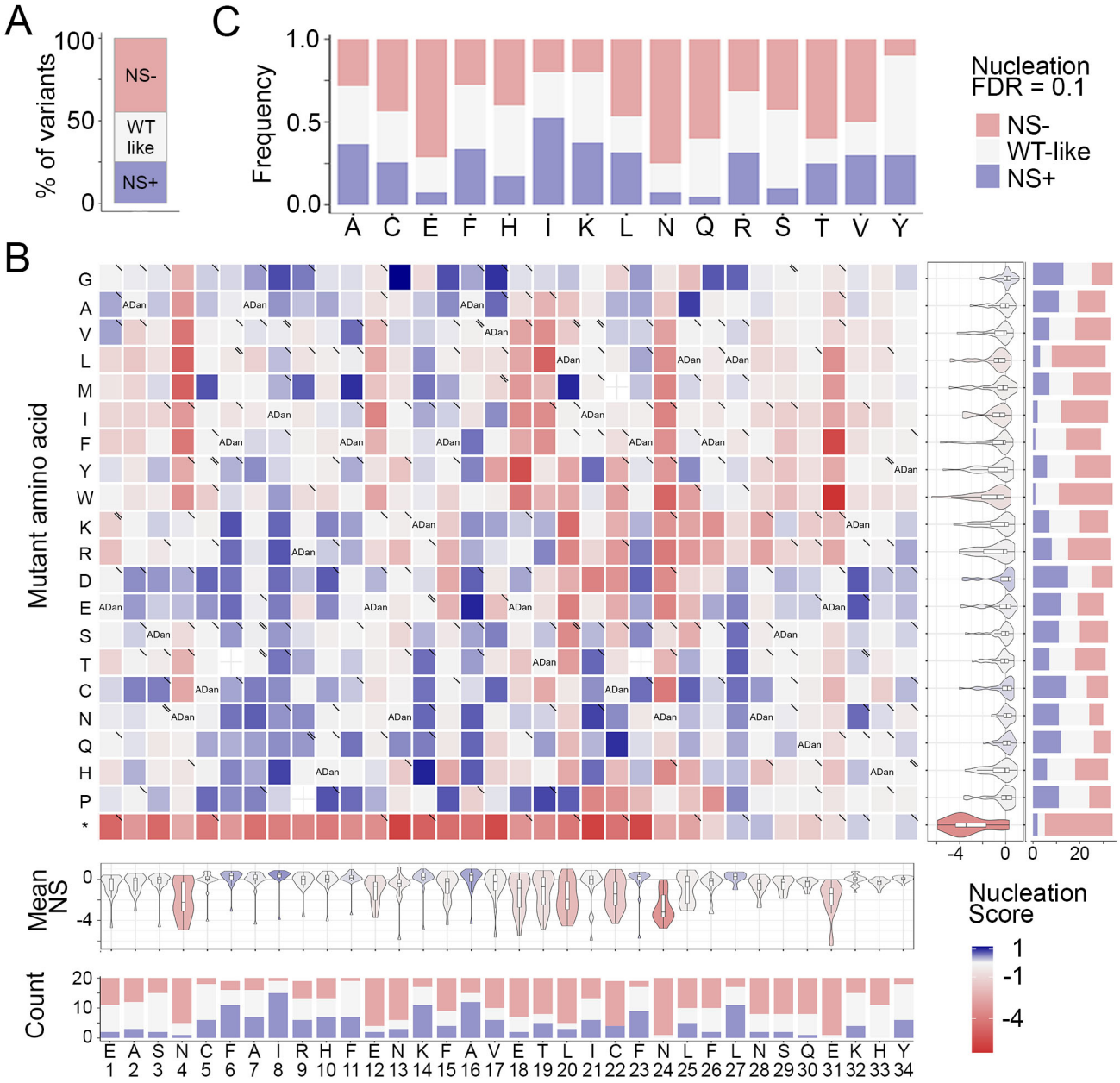
A
% of variants
100
50
0
NS-
WT like
NS+
C
Frequency
1.0
0.5
0.0
A C E F H I K L N Q R S T V Y
Nucleation FDR = 0.1
NS-
WT-like
NS+
B
Mutant amino acid
G A V L M I F Y W K R D E S T C N Q H P *
ADan
Mean NS
0
-4
Count
20
10
0
E A S N C F A I R H F E N K F A V E T L I C F N L F L N S Q E K H Y
1 2 3 4 5 6 7 8 9 10 11 12 13 14 15 16 17 18 19 20 21 22 23 24 25 26 27 28 29 30 31 32 33 34
-4 0
0 20
Nucleation Score
1
-1
-4

Figure 3

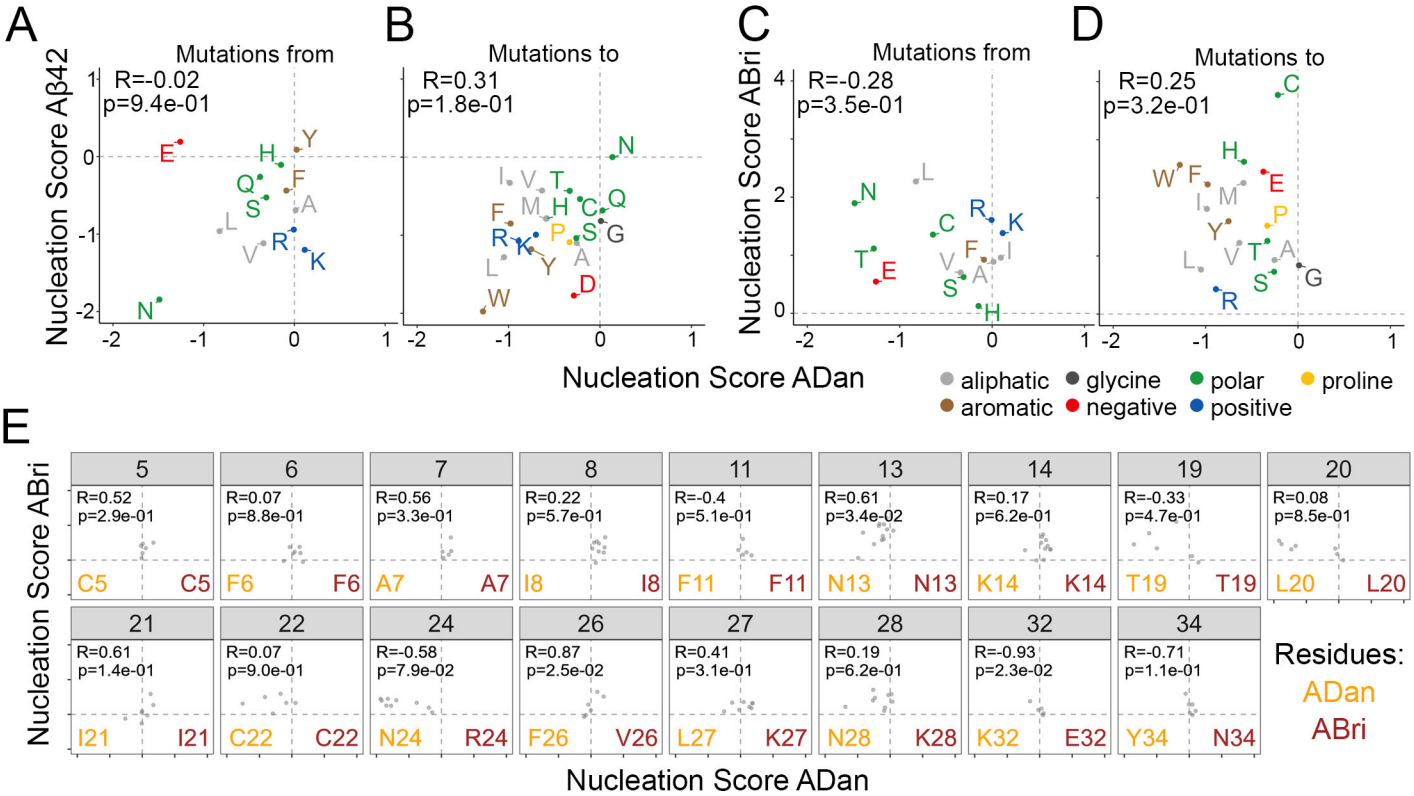
A
Mutations from
R=-0.02
p=9.4e-01
Nucleation Score Aβ42
B
Mutations to
R=0.31
p=1.8e-01
C
Mutations from
R=-0.28
p=3.5e-01
Nucleation Score ABri
D
Mutations to
R=0.25
p=3.2e-01
Nucleation Score ADan
aliphatic
glycine
polar
proline
aromatic
negative
positive

E
Nucleation Score ABri
5 R=0.52 p=2.9e-01 C5 C5
6 R=0.07 p=8.8e-01 F6 F6
7 R=0.56 p=3.3e-01 A7 A7
8 R=0.22 p=5.7e-01 I8 I8
11 R=-0.4 p=5.1e-01 F11 F11
13 R=0.61 p=3.4e-02 N13 N13
14 R=0.17 p=6.2e-01 K14 K14
19 R=-0.33 p=4.7e-01 T19 T19
20 R=0.08 p=8.5e-01 L20 L20
21 R=0.61 p=1.4e-01 I21 I21
22 R=0.07 p=9.0e-01 C22 C22
24 R=-0.58 p=7.9e-02 N24 R24
26 R=0.87 p=2.5e-02 F26 V26
27 R=0.41 p=3.1e-01 L27 K27
28 R=0.19 p=6.2e-01 N28 K28
32 R=-0.93 p=2.3e-02 K32 E32
34 R=-0.71 p=1.1e-01 Y34 N34
Residues:
ADan
ABri
Nucleation Score ADan

Figure 4

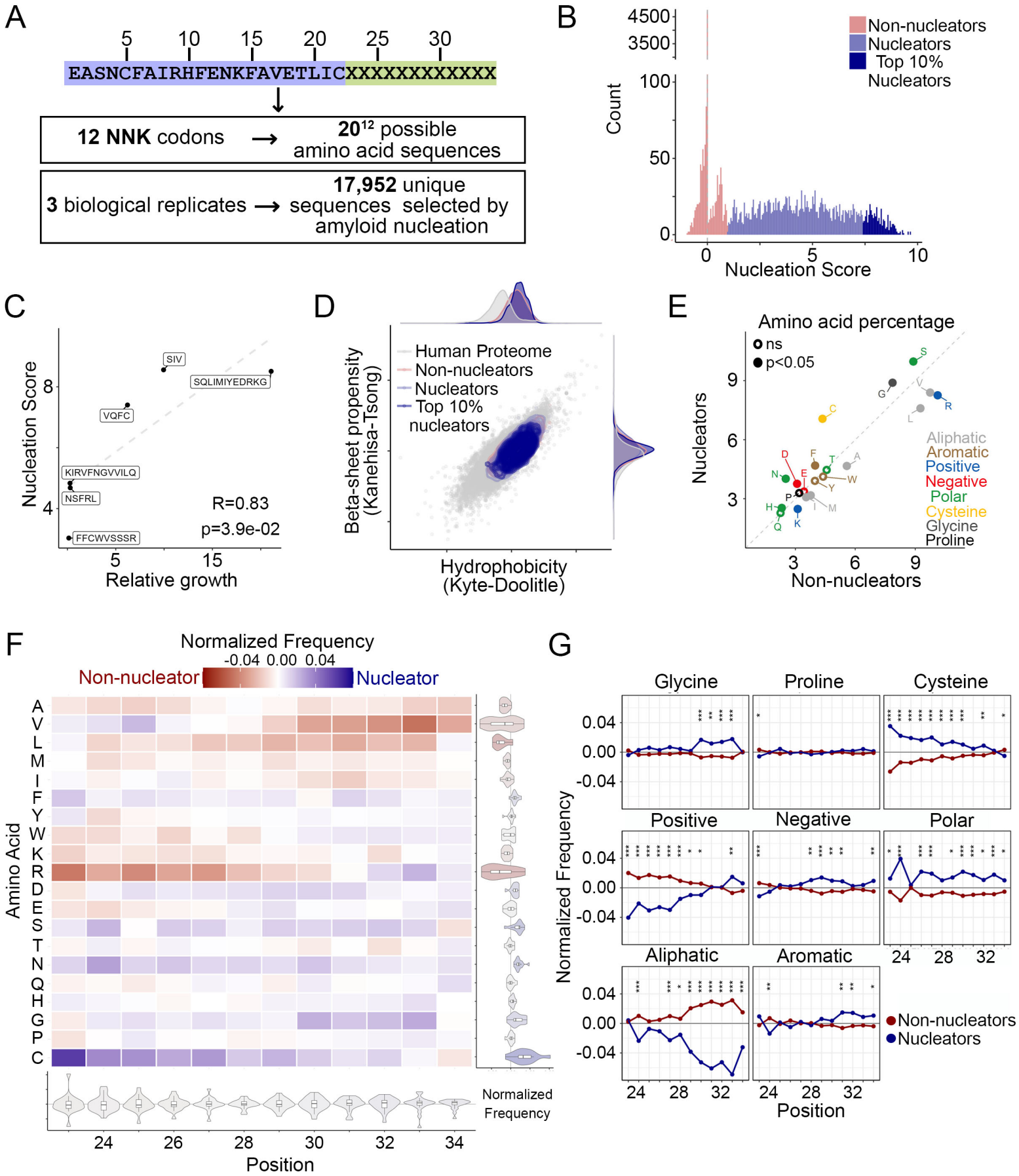
A
5 10 15 20 25 30
EASNCFAIRHFENKFAVETLICXXXXXXXXXXXX
12 NNK codons → 20^12 possible amino acid sequences
3 biological replicates → 17,952 unique sequences selected by amyloid nucleation
B
Non-nucleators
Nucleators
Top 10% Nucleators
Count
Nucleation Score
C
Nucleation Score
Relative growth
SIV
SQLIMIYEDRKG
VQFC
KIRVFNGVVILQ
NSFRL
FFCWVSSSR
R=0.83
p=3.9e-02
D
Human Proteome
Non-nucleators
Nucleators
Top 10% nucleators
Beta-sheet propensity (Kanehisa-Tsong)
Hydrophobicity (Kyte-Doolitle)
E
Amino acid percentage
ns
p<0.05
Nucleators
Non-nucleators
Aliphatic
Aromatic
Positive
Negative
Polar
Cysteine
Glycine
Proline
F
Normalized Frequency
Non-nucleator
Nucleator
Amino Acid
Position
Normalized Frequency
G
Glycine
Proline
Cysteine
Positive
Negative
Polar
Aliphatic
Aromatic
Normalized Frequency
Position
Non-nucleators
Nucleators

Figure 5

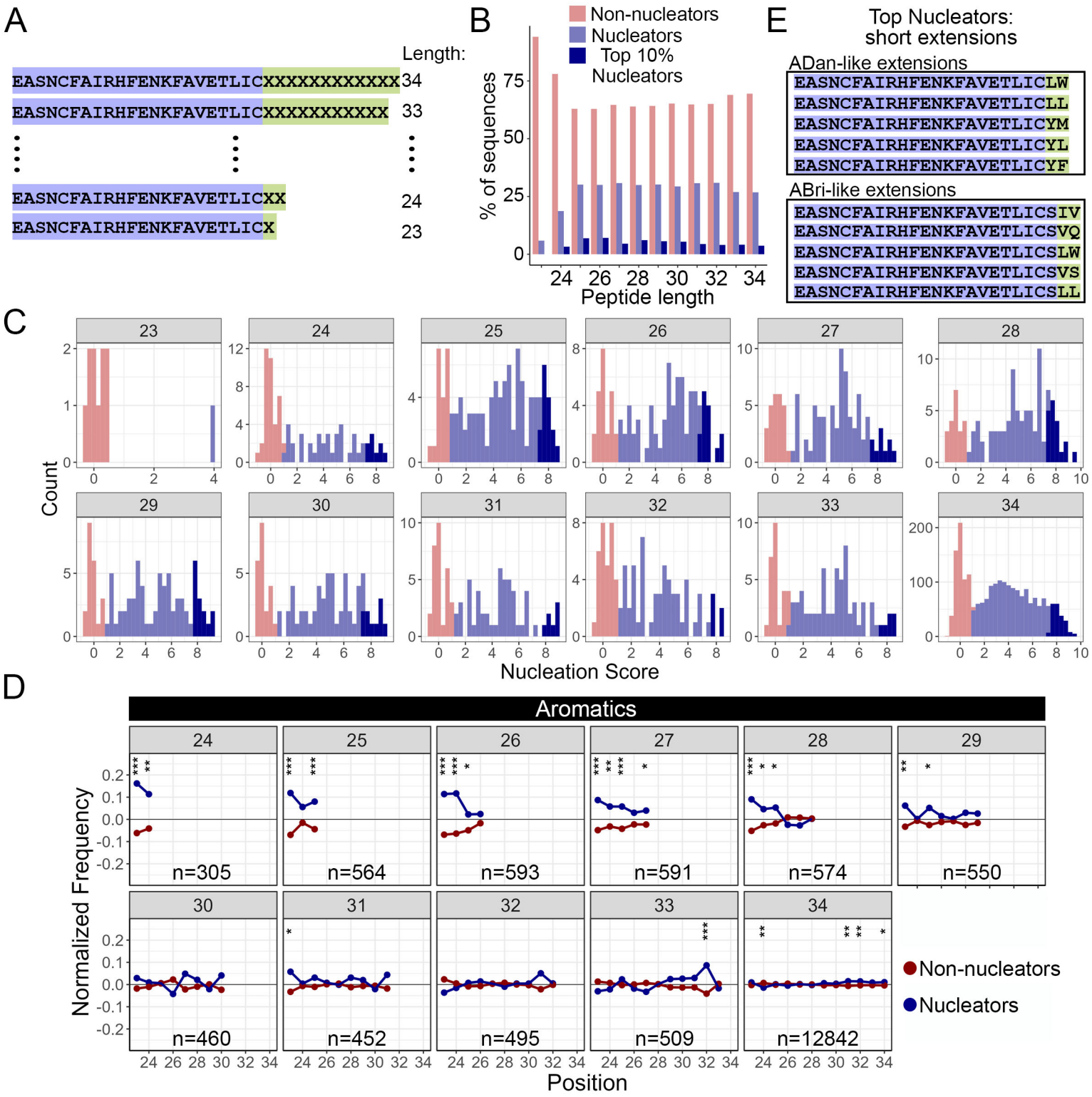
A
Length:
EASNCFAIRHFENKFAVETLICXXXXXXXXXXXX 34
EASNCFAIRHFENKFAVETLICXXXXXXXXXXX 33
EASNCFAIRHFENKFAVETLICXX 24
EASNCFAIRHFENKFAVETLICX 23
B
Non-nucleators
Nucleators
Top 10% Nucleators
% of sequences
Peptide length
E
Top Nucleators: short extensions
ADan-like extensions
EASNCFAIRHFENKFAVETLICLW
EASNCFAIRHFENKFAVETLICLL
EASNCFAIRHFENKFAVETLICYM
EASNCFAIRHFENKFAVETLICYL
EASNCFAIRHFENKFAVETLICYF
ABri-like extensions
EASNCFAIRHFENKFAVETLICSIV
EASNCFAIRHFENKFAVETLICSVQ
EASNCFAIRHFENKFAVETLICSLW
EASNCFAIRHFENKFAVETLICSVS
EASNCFAIRHFENKFAVETLICSLL
C
Count
Nucleation Score
D
Aromatics
Normalized Frequency
n=305
n=564
n=593
n=591
n=574
n=550
n=460
n=452
n=495
n=509
n=12842
Position
Non-nucleators
Nucleators

Supplementary Figure 1

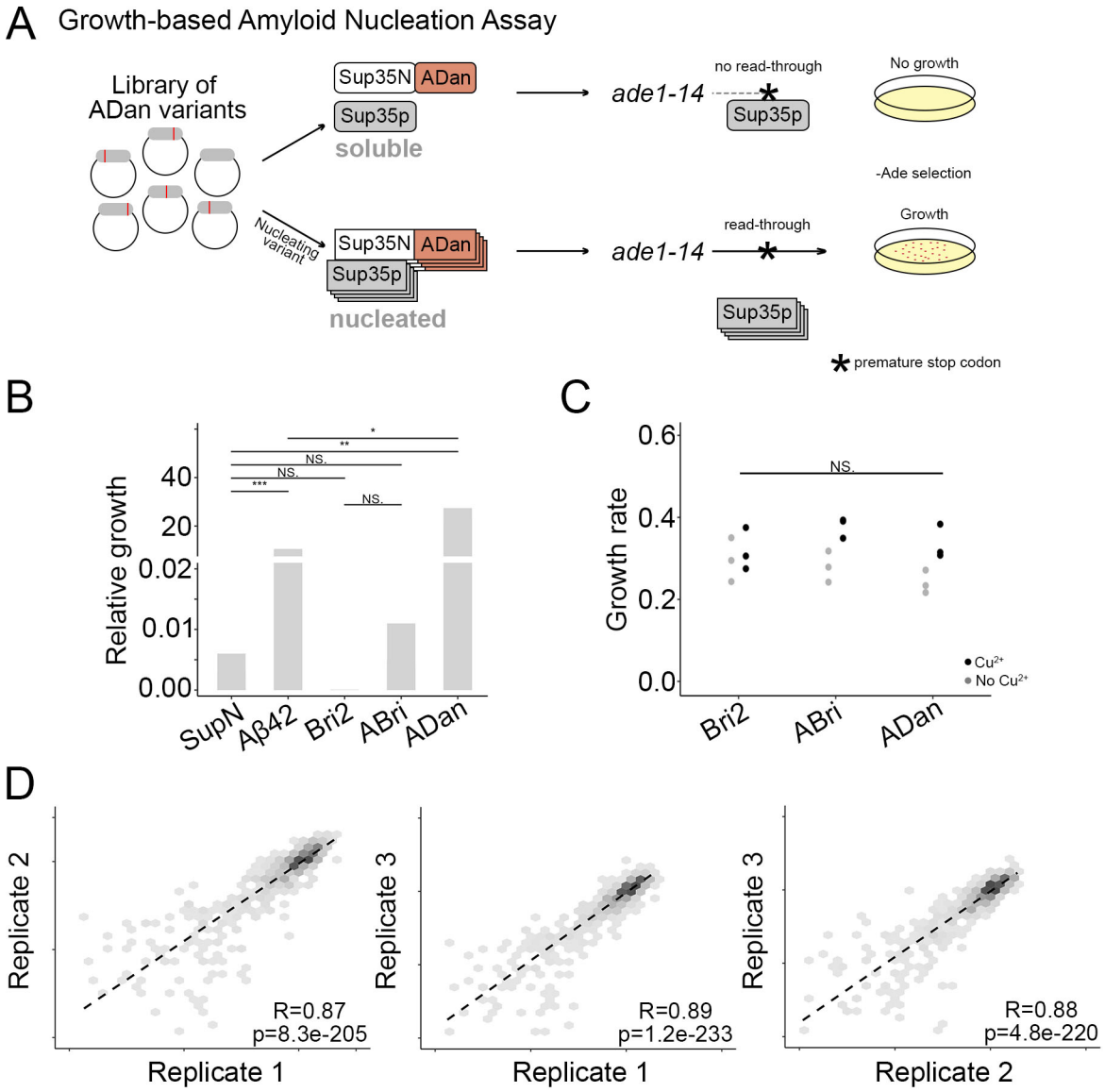

Supplementary Figure 2

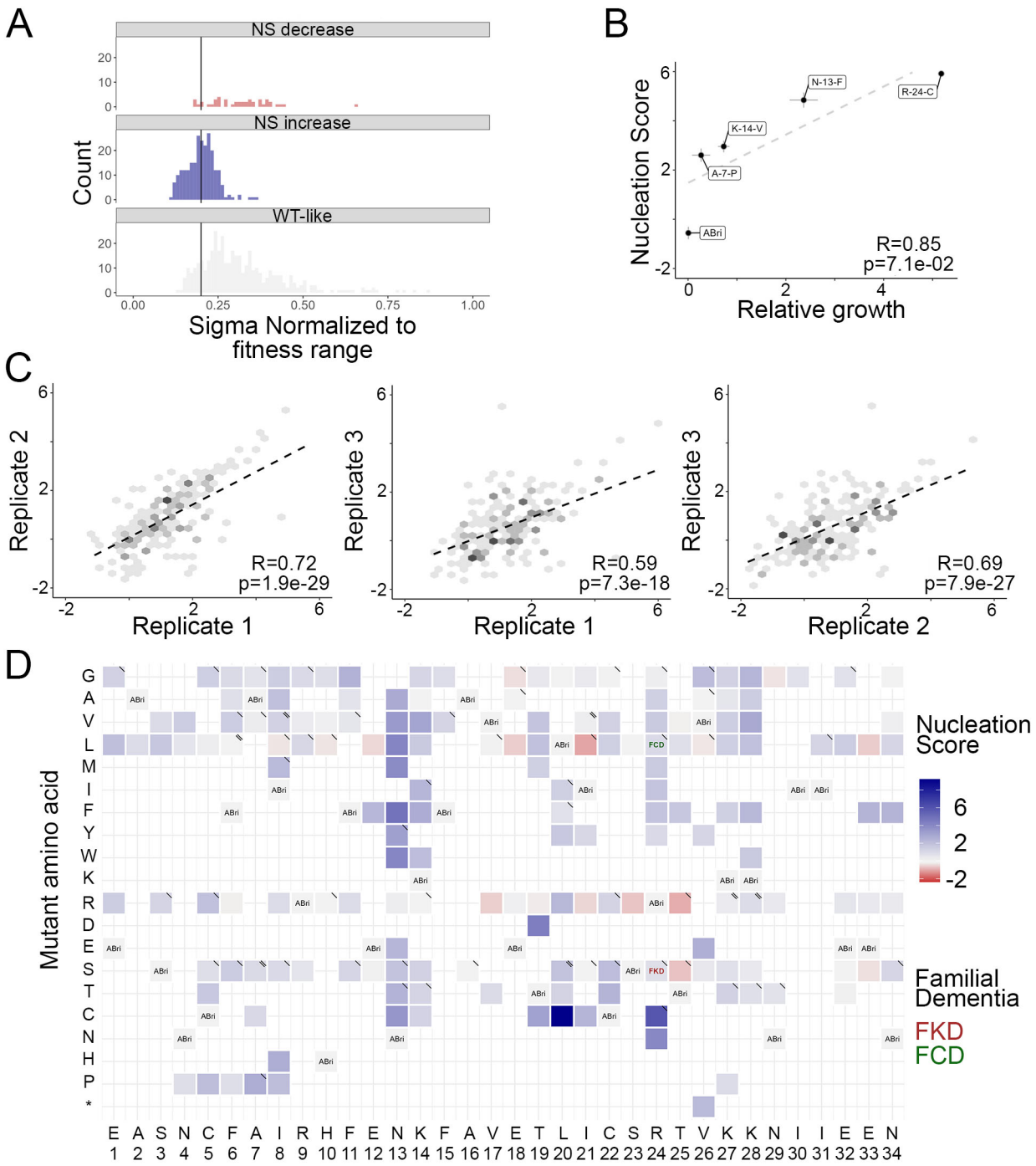

Supplementary Figure 3

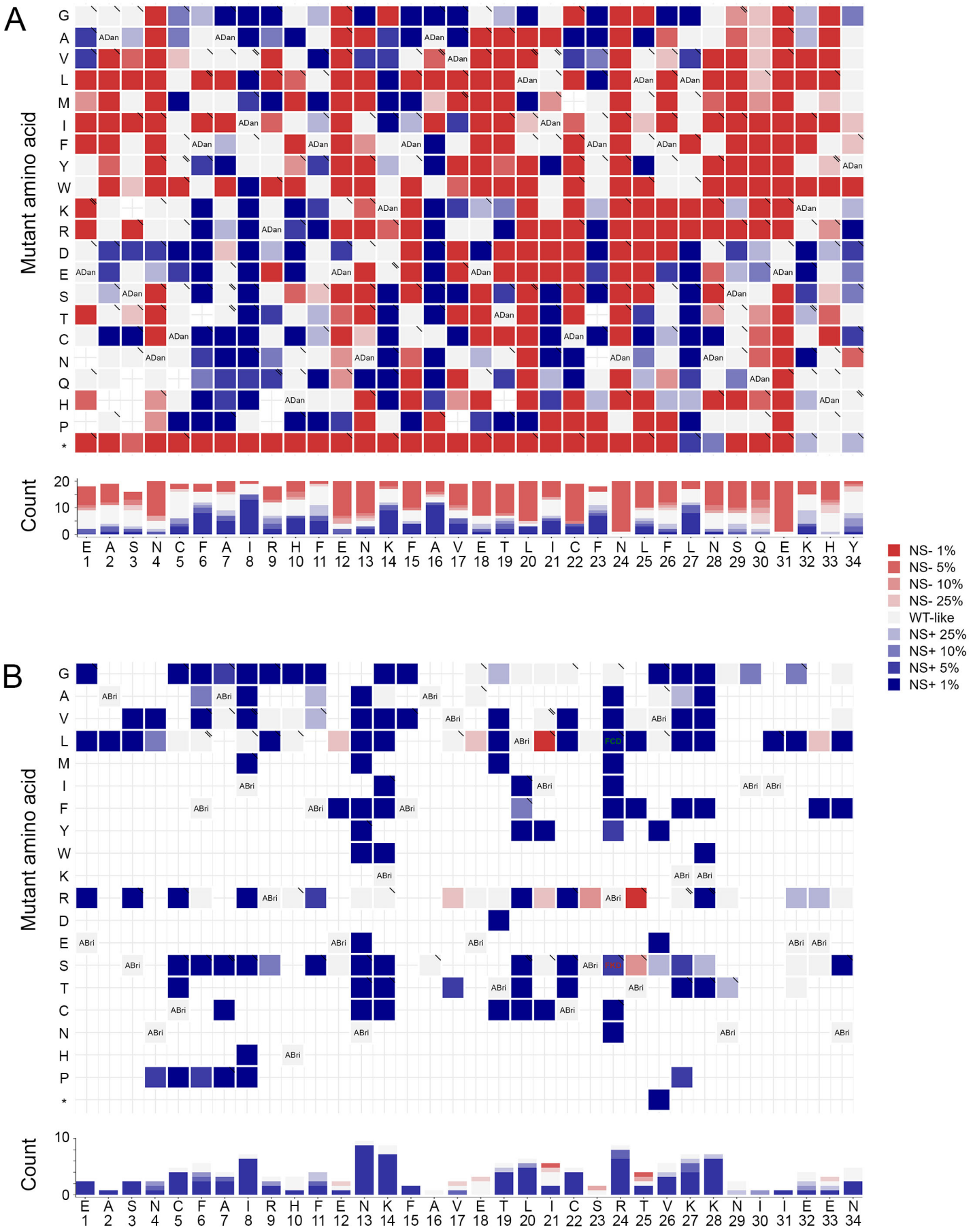

Supplementary FIgure 4

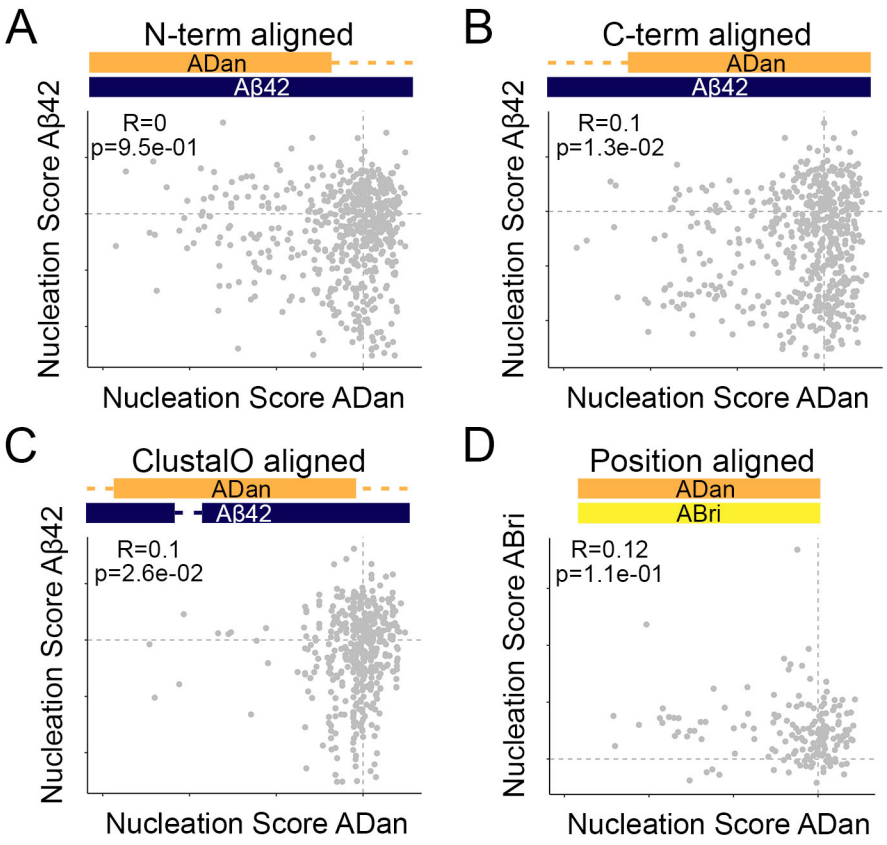

Supplementary Figure 5

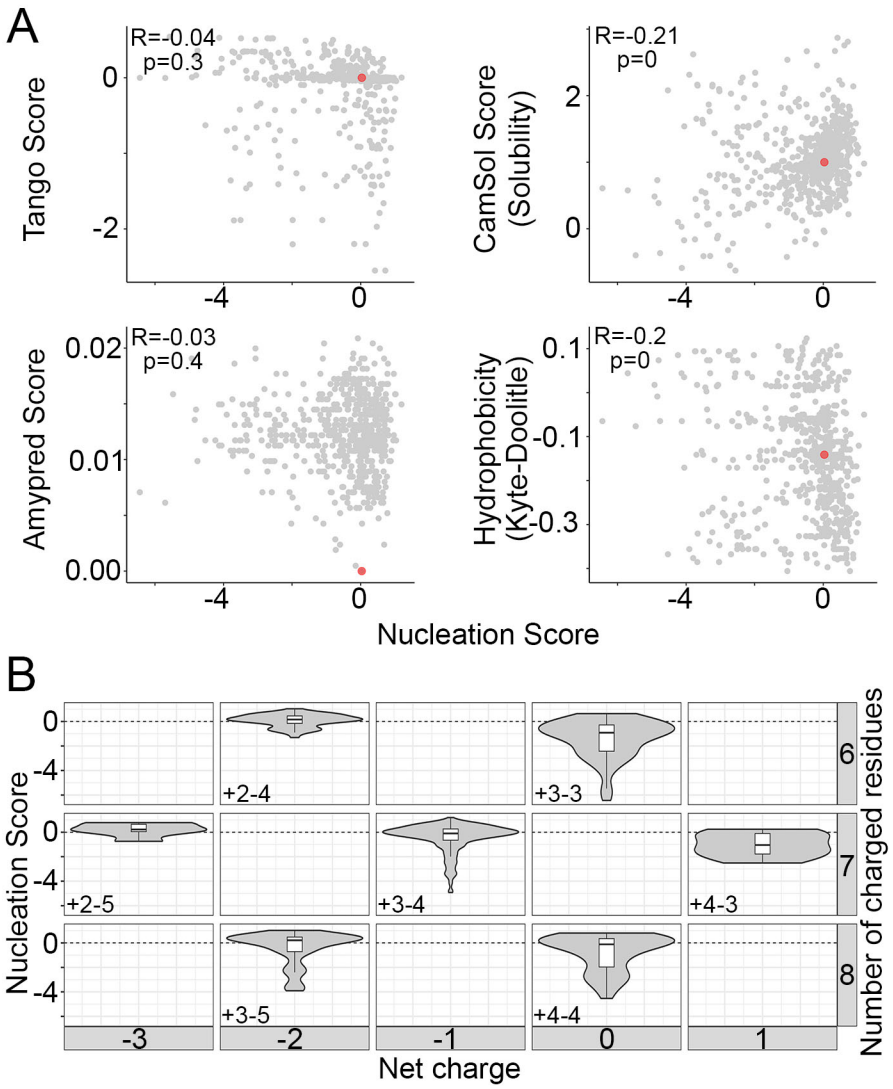

Supplementary Figure 6

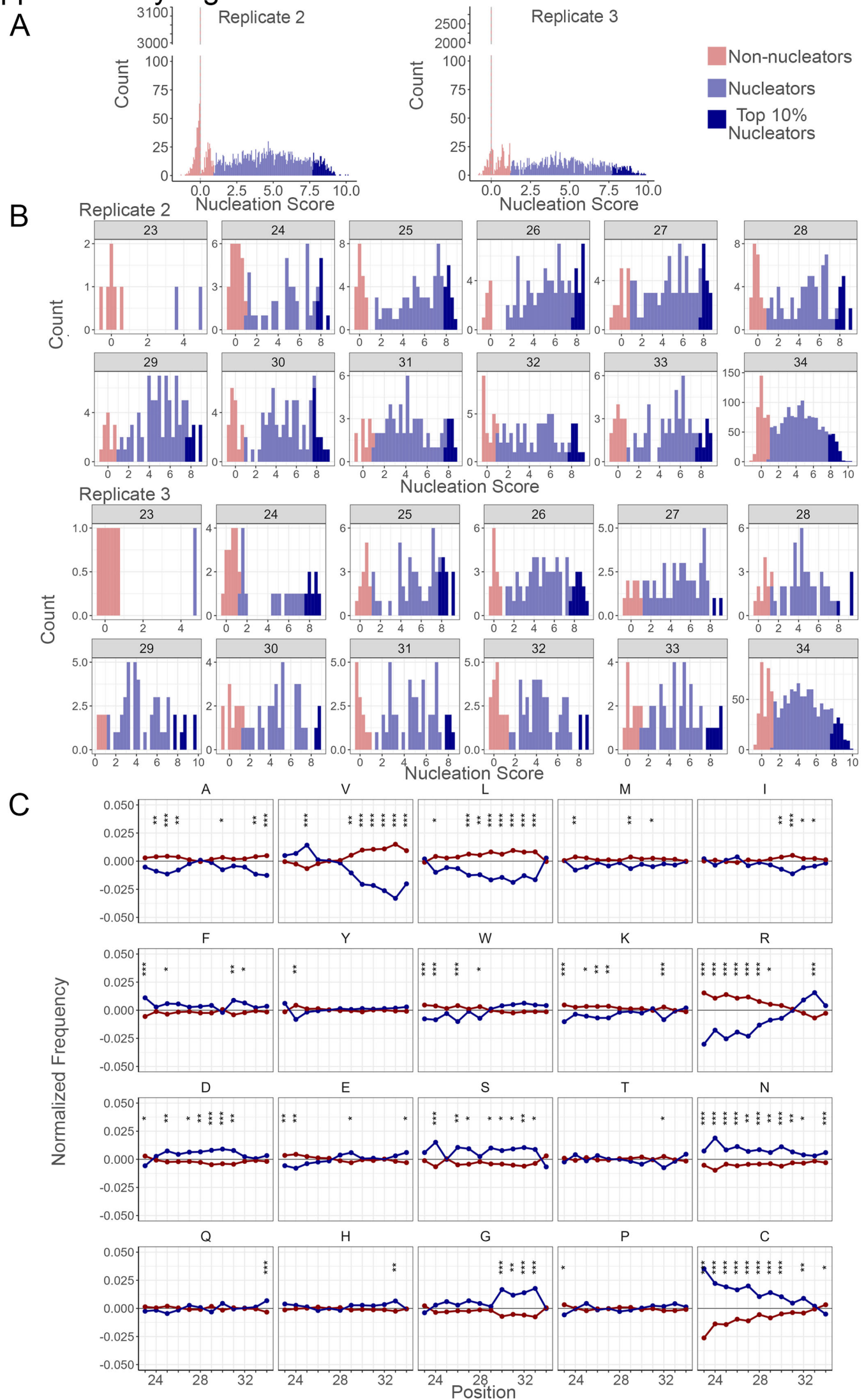

Supplementary Figure 7

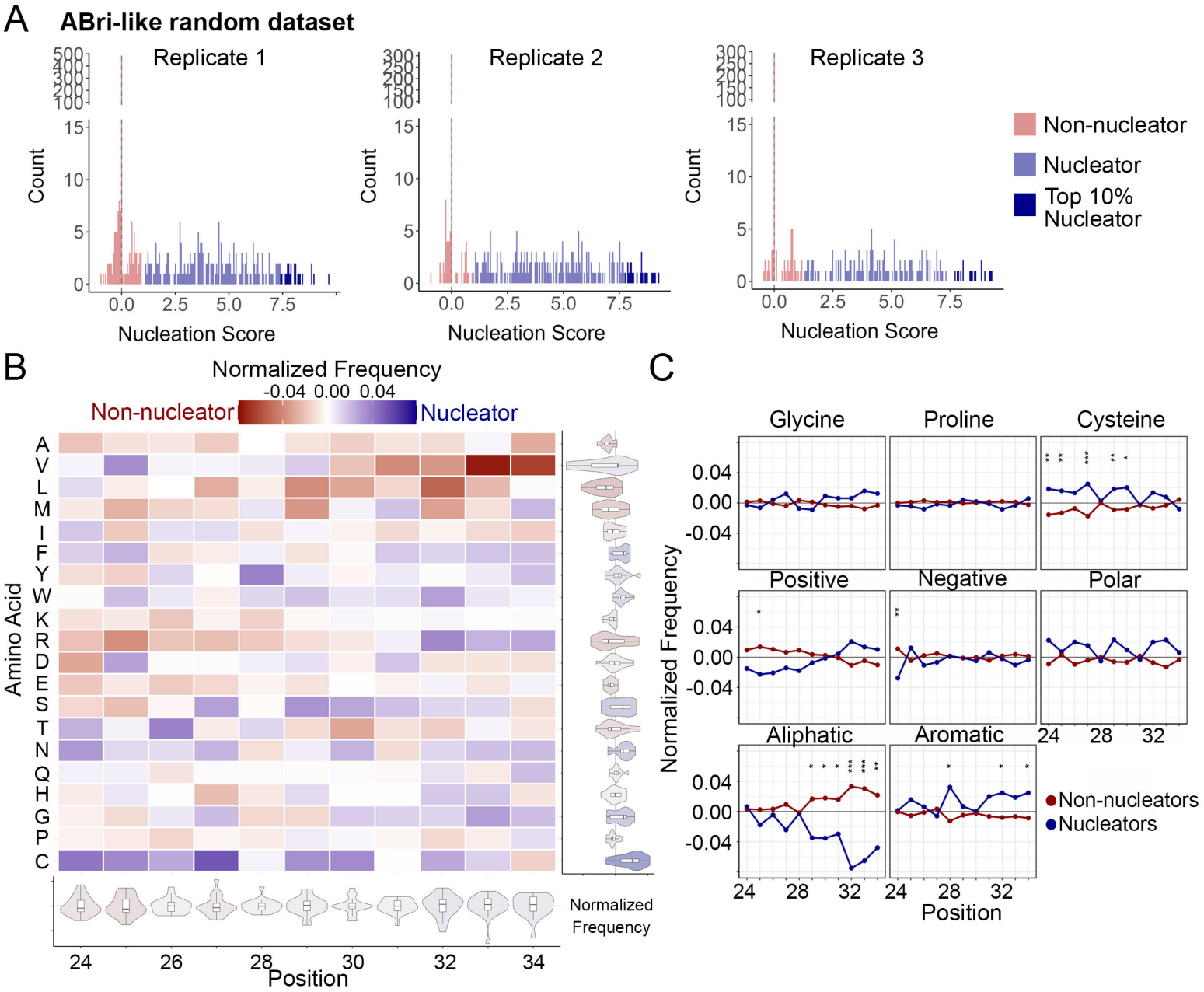

Supplementary Figure 8

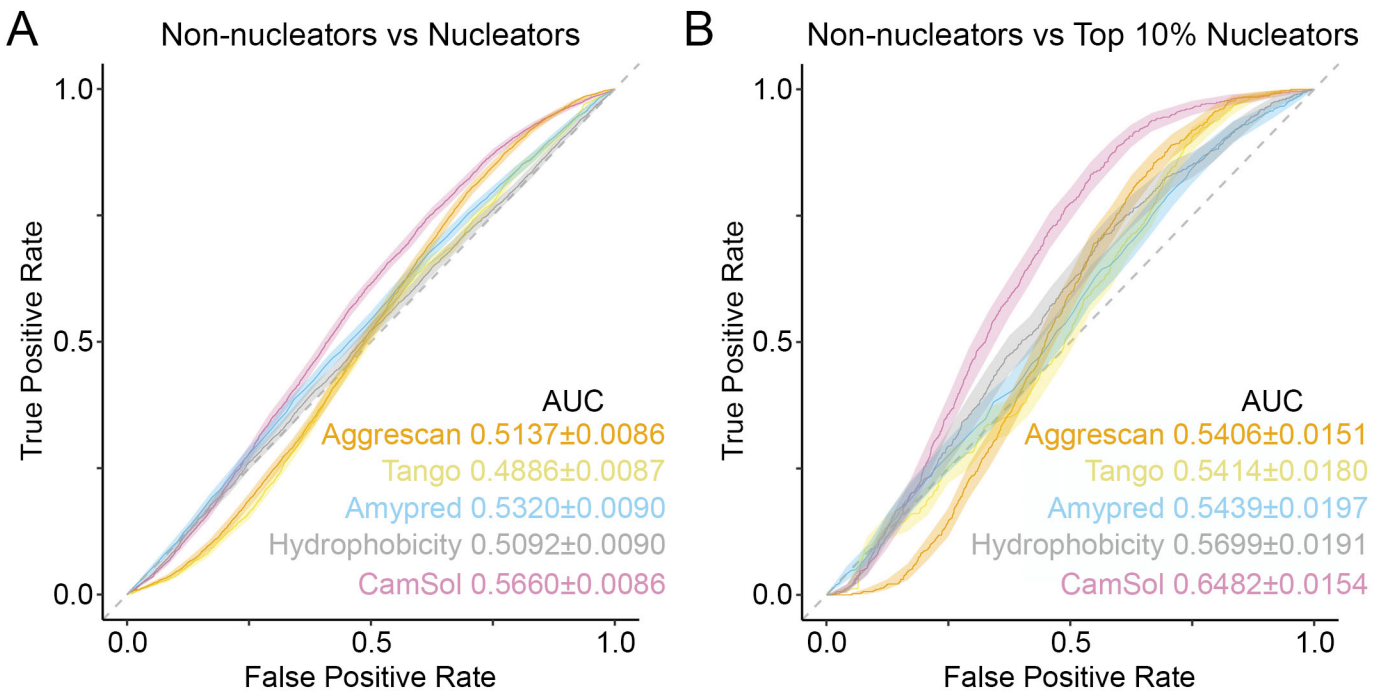
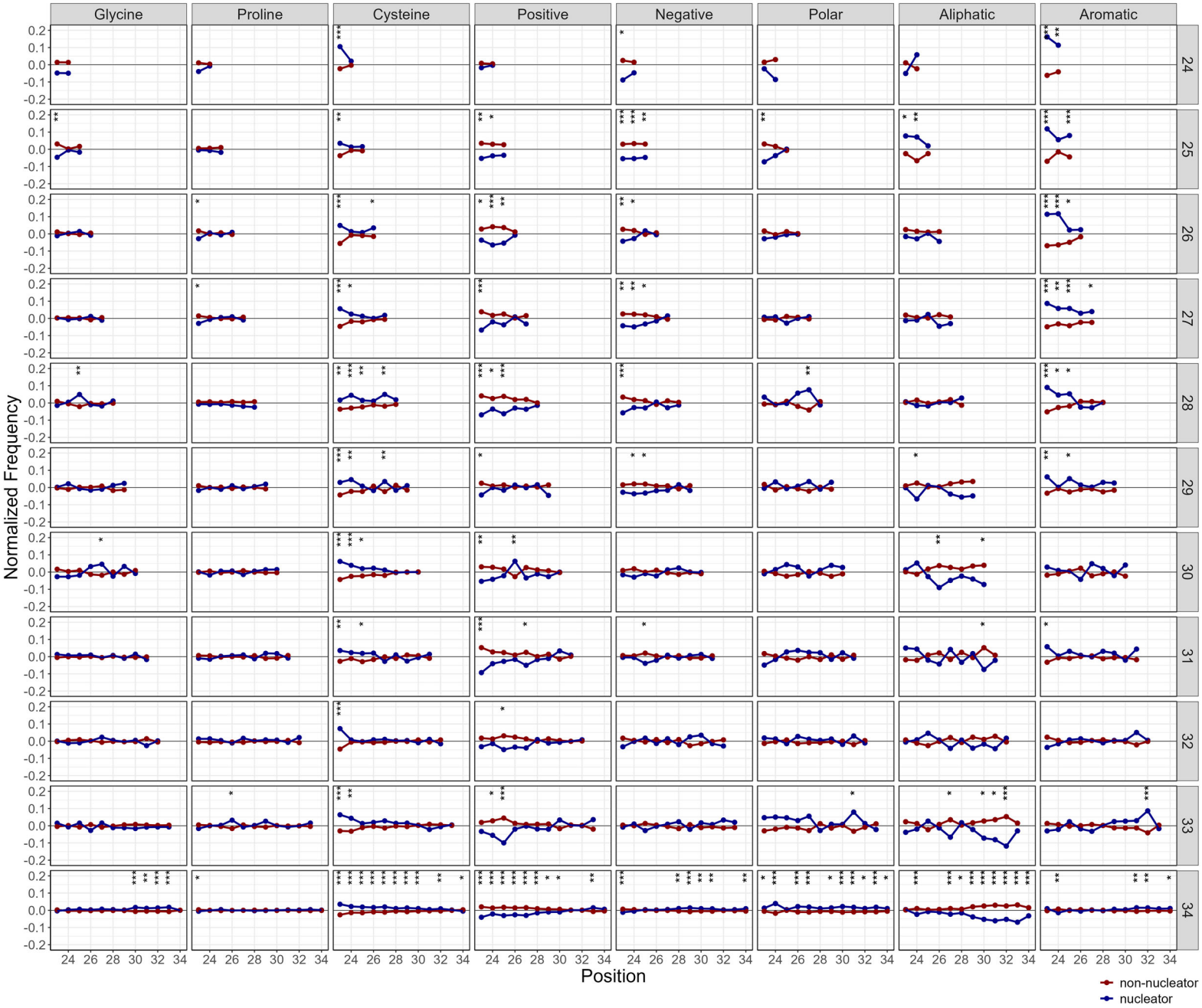
Supplementary Figure 9